Oxide Perovskites, Double Perovskites and Derivatives for Electrocatalysis, Photocatalysis, and Photovoltaics

Journal:	*Energy & Environmental Science*
Manuscript ID	EE-REV-05-2018-001574.R2
Article Type:	Review Article
Date Submitted by the Author:	01-Aug-2018

Complete List of Authors:	Yin, Wanjian; Soochow University, School of Energry Weng, Baicheng; University of Toledo Ge, Jie; Seoul National University, Department of Materials Science and Engineering sun, de; Soochow Institute for Energy and Materials InnovationS (SIEMIS), Li, Zhenzhu; Soochow University, College of Physics, Optoelectronics and Energy of Soochow University Yan, Yanfa; University of Toledo, Department of Physics and Astronomy

Oxide Perovskites, Double Perovskites and Derivatives for Electrocatalysis, Photocatalysis, and Photovoltaics

Wan-Jian Yin[1,2#], Baicheng Weng[3#], Jie Ge[4,5#], Qingde Sun[1,2], Zhenzhu Li[1,2], Yanfa Yan[3,*]

[1]College of Energy, Soochow Institute for Energy and Materials InnovationS (SIEMIS), Soochow University, Suzhou 215006, China.

[2]Key Laboratory of Advanced Carbon Materials and Wearable Energy Technologies of Jiangsu Province, Soochow University, Suzhou 215006, China.

[3]Department of Physics and Astronomy, and Wright Center for Photovoltaics Innovation and Commercialization, The University of Toledo, Toledo, Ohio 43606, United States

[4]SNU Materials Division for Educating Creative Global Leaders, Seoul National University, Seoul 08826, Republic of Korea

[5]Institute of Physics, Martin-Luther-University Halle-Wittenberg, 06120 Halle, Germany

Email: yanfa.yan@utoledo.edu

#These authors contributed equally.

Broader Context

Clean energy conversion is crucial to sustain the rapid development of human society and mitigate the greenhouse effect and environmental pollution from fossil fuel. Practical utilization of clean energies requires the energy conversions involving different process such as photovoltaics (PV, from solar energy to electrical energy), electrocatalysis (EC, from electrical energy to chemical energy), photocatalysis (PC, from solar energy to chemical energy). A key issue to realize high-efficiency conversion process is to search stable, low-cost and environment-friendly functional materials. Due to the extreme structural and compositional flexibilities, oxide perovskites and their derivates are attractive candidates for the diverse applications aforementioned. This paper reviews the structural and compositional flexibility oxide perovskites and their derivatives and the progress of their applications in clean energy conversion. It attempts to describe how the properties of oxide perovskites and their derivates are tuned for specific applications.

Abstract

Searching for novel functional materials represents an important direction in the research and development of renewable energy. Due to the unique structural and compositional flexibility and high material stability, oxide perovskites and their derivatives have recently been extensively explored as a class of versatile materials for applications in electrocatalysis (EC), photocatalysis (PC) and photovoltaics (PV), showing great promises in catalytic activity and device stability. In this review, we firstly discuss the extreme flexibilities of oxide perovskites in terms of their structures and compositions, which lead to a treasure trove of materials for diverse applications. Secondly, the current status of their applications and challenges in EC, PC and PV are reviewed. We attempt to build the connections between the structural and compositional flexibility and the tunable materials properties desirable for various applications.

1. Introduction

The rapidly growing global demand on energy and extensive concerns about the greenhouse effect and environmental pollution from fossil energy production have stimulated intensive research interest in the generation of sustainable and clean energies and new electrochemical energy storage systems[1-13]. Converting solar energy to electricity or chemical fuels represents the forefront of renewable energy research. Whereas, photovoltaics (PV) uses semiconductors to absorb sunlight and directly convert solar energy into electricity, eletrocatalysis (EC) uses electrons to reduce water or CO_2 to generate valuable clean and storable H_2 or CO, alcohols and hydrocarbon fuels. Photocatalysis (PC) including photoelectrochemical (PEC) catalysis and

non-PEC photocatalysis[14, 15] further employs semiconductors to absorb sunlight to create charge pairs for realizing water splitting and CO_2 reduction. Fuel cells and metal-air batteries use EC to reduce earth-abundant oxygen at the cathode and evolve oxygen at the anode for generating electricity.[8,16]

Before large-scale applications can be realized, several key challenges must be overcome, including high-cost, poor stability and sluggish performance of catalysts as well as weak absorption of photoabsorbers. For instance, the lack of low-cost electrocatalysts consisting of earth-abundant elements with superior oxygen evolution reaction (OER) activity and stability than the current noble metal catalysts, IrO_2 and RuO_2, hurdles the practical application of water splitting at large scale[17]. The commercialization of metal-air batteries is hindered by the high-cost, high overpotential and low rate-capacity of platinum catalyst, as well as the sluggish oxygen reduction reaction (ORR) at the cathode[8]. As for CO_2 reduction, the electrochemical production of C2 or C3 (such as ethylene, ethanol and n-propanol) fuels is still not able to compete with chemical synthesis processes[18]. To date, few *n*-type photoanodes have demonstrated long-term and efficient oxygen production for PEC water oxidation. Most non-oxide *n*-type semiconductors are chemically unstable in aqueous solutions and form thick oxide layers that block the OER. The more promising materials for producing stable and oxidation-resistant photoanodes are metal oxides. Unfortunately, none of the current existing metal oxides have demonstrated high solar-to-hydrogen conversion efficiencies under visible light irradiation, although many of them are stable in aqueous solutions and are resistant to oxidation. This underperformance is due largely to the fact that most metal oxides have too large bandgaps to effectively absorb the main portion of the sunlight spectrum, *i.e.*, visible light[19-21]. While EC and PC involve functional materials for the OER, ORR, hydrogen evolution reaction (HER) and CO_2 reduction reaction (CO_2RR), PV usually does not involve chemical reactions.

Recently, extensive efforts have been made to address the aforementioned issues through developing new functional materials. Since the energy conversion processes in different technologies are different, the functional materials used in these technologies require rather different materials properties. Nevertheless, it is interesting to note that a class of materials, namely, oxide perovskites and their derivatives[17, 19-24], can be used in all these technologies, reflecting their versatile properties. Additionally, oxide perovskites exhibit several other attractive properties[25, 26] including superconductivity, ferroelectricity, magnetoresistance and ionic conductivity, owing to their structural and compositional flexibility. Recently, halide perovskites have attracted global interest in PV applications[27-30] due to their superior photovoltaic properties such as extremely high optical absorption coefficient, super long carrier diffusion length and low-temperature solution processability. However, the practical use of halide perovskites in these technologies are rather challenging due to the instabilities to moisture, temperature, and environment. In contrast, oxide perovskites and the derivatives have exhibited broader applications in EC, PC, and PV owing to their superior stability. Here, we provide a review on the structural and compositional flexibility of oxide perovskites and derivatives and the status of their applications in EC (i.e. OER, ORR, HER and CO_2RR), PC and PV. The challenge and perspective will also be discussed.

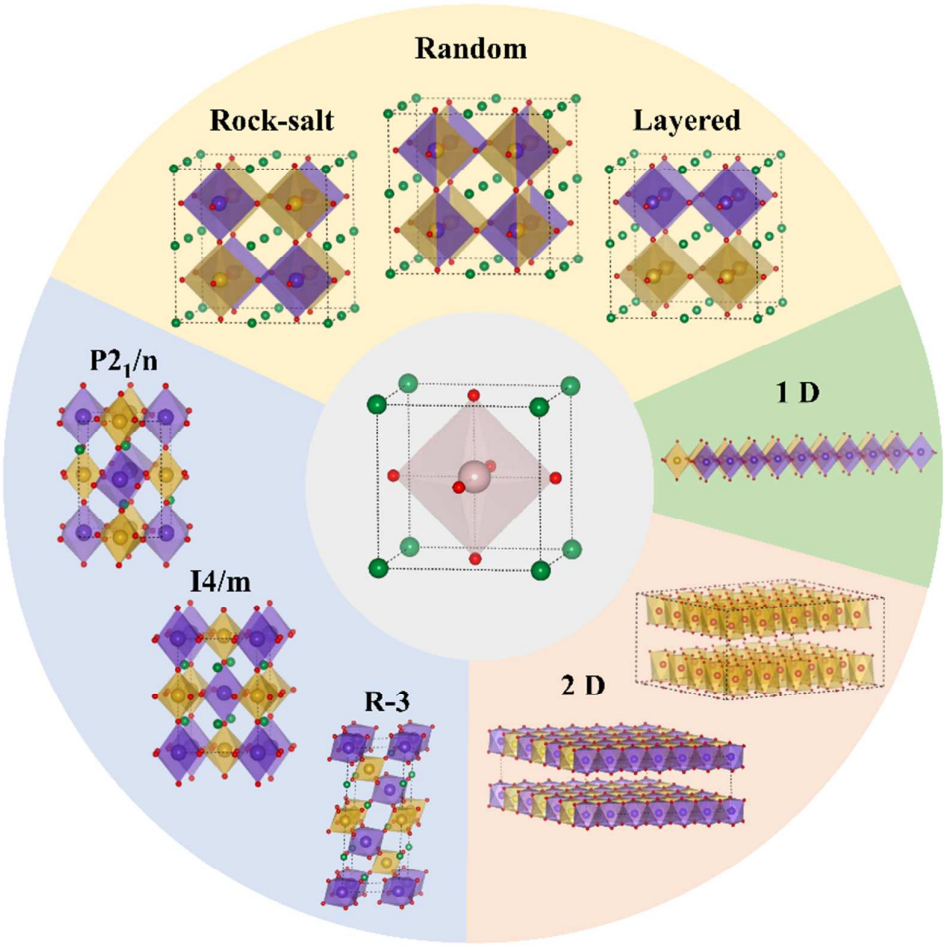

Fig. 1 The structural flexibility of oxide perovskites. From single cubic perovskite (center) to double cubic perovskite with the B-site ordering of rock-salt, random and layered structure (see Table 1 for detailed information). Through [BO_6] octahedral tilt, cubic phases can transform to different tilted phases with three dominating ones shown on down left. Under large distortion of [BO_6] octahedra, the three-dimensional (3D) connection of octahedra can be broken, leading to 2D and 1D perovskite derivatives.

Tab. 1 Crystallographic information for common double perovskites.[31]

sublattice type	cell size	crystal system	space group
random	$1a_p \times 1a_p \times 1a_p$	cubic	$Pm\bar{3}m$
	$\sqrt{2}a_p \times \sqrt{2}a_p \times 2a_p$	orthorhombic	Pbnm
rock salt	$2a_p \times 2a_p \times 2a_p$	cubic	$Fm\bar{3}m$
	$\sqrt{2}a_p \times \sqrt{2}a_p \times 2a_p$	monoclinic	$P2_1/n$
layered	$2a_p \times 2a_p \times 2a_p$	monoclinic	$P2_1/m$

2. Structural and Compositional Flexibility of Oxide Perovskites

2.1 Structural flexibility

2.1.1 Single Perovskites

Perovskites with a general formula ABX_3, in which A and B are large electropositive cations and X is an anion, have the structure shown at the center of Figure 1. The ideal oxide perovskite ABO_3 has the cubic structure with a high symmetry of $Pm\bar{3}m$, comprising of a highly flexible

framework built up from chains of corner-sharing [BO_6] octahedra and A cations occupying the resulting holes with cuboctahedra symmetry. Cubic phase is usually observed at high temperatures above 1000 K for oxide perovskites[32]. When temperature goes down, cubic perovskites undergo octahedral rotations along its symmetry axes ([100], [010], [001]) and change to lower-symmetry phases[33, 34]. To have a complete picture of perovskite tilt, Glazer developed a method to describe the octahedral tilting in perovskites in 1970*s*[35] *i.e.*, combining the rotations along the three orthogonal symmetry axes of the octahedra. At that time, twenty-three kinds of crystal structures for tilt perovskites were identified, while further group theory analysis led to only fifteen unique tilt patterns[36] as shown in Table 2. A comprehensive literature survey[37] showed that 90% single oxide perovskites adopt only four kinds of Glazer tilt, corresponding to four common phases as shown in Table 3.

Tab. 2 Notations of Glazer, the space group symmetries, and numbers of ABX_3 formula units in the primitive cell (N) of fifteen possible tilts for single perovskites.[34]

	Tilts	Space-group	N
zero-tilt	$(a^0a^0a^0)$	$Pm\bar{3}m$(#221)	1
One-tilt	$(a^0a^0c^-)$	I4/mcm(#140)	4
	$(a^0a^0c^+)$	P4/mbm(#127)	2
two-tilt	$(a^0b^-b^-)$	Imma(#74)	4
	$(a^0b^-c^-)$	C2/m(#12)	4
	$(a^0b^+c^-)$	Cmcm(#63)	8
	$(a^0b^+b^+)$	I4/mmm(#139)	8
three-tilt	$(a^-a^-a^-)$	$R\bar{3}c$(#167)	6
	$(a^-b^-b^-)$	C2/c(#15)	8
	$(a^-b^-c^-)$	P1(#2)	8
	$(a^+b^-b^-)$	Pnma(#62)	4
	$(a^+b^-c^-)$	$P2_1/m$(#11)	8
	$(a^+a^+c^-)$	$P4_1/nmc$(#137)	8
	$(a^+a^+a^+)$	$Im\bar{3}$(#204)	8
	$(a^+b^+c^+)$	Immm(#71)	8

2.1.2 Double Perovskites

Double perovskites describe the perovskites with A or B site occupied by two different types of cations, giving the formulas of $A'A''B_2O_6$ (double A-site) or $A_2B'B''O_6$ (double B-site). Since A-site cations usually act as electron donor to the [BO_6] framework and the physical properties of ABO_3 perovskites are highly dependent on B-site cations, double perovskites usually indicate double B-site perovskites. Hereafter, 'perovskite/double perovskite' indicates 'oxide perovskite/oxide double perovskite' unless specifically stated otherwise.

The crystal structure of a double perovskite $A_2B'B''O_6$ is determined by the arrangement of B′ and B″ cations in B sublattice. Due to the charge (size) difference between B′ and B″ cations, the Madelung (strain) energy of double perovskites $A_2B'B''O_6$ can be reduced by the particular ordering on B-site. There are mainly three kinds of B-cation sublattice[31] including random, rock salt and layered structure as shown in Figure 1 and Table 1. The types of arrangements are generally determined by the charge difference (ΔQ) between B′ and B″. Based on the existing

double perovskites, the random order dominates when ΔQ = 1, but the rock-salt order dominates when ΔQ > 2. This could be explained by larger Madelung energy for random order for a larger ΔQ. Since ΔQ > = 2 in most of double perovskites, the rock-salt order accounts for the majority of double perovskites.

Tab. 3 Four common phases for single and double oxide perovskites. The frequency means the number of perovskites adopting corresponding phases. The data are from Refs [33, 37].

	Single perovskite		Double perovskite	
Glazer notation	Space group	Frequency	Space group	Frequency
$a^-a^-b^+$	$Pnma$	119	$P2_1/n$	168
$a^0a^0a^0$	$Pm\bar{3}m$	21	$Fm\bar{3}m$	94
$a^0a^0c^-$	$I4/mcm$	9	$I4/m$	27
$a^-a^-a^-$	$R\bar{3}c$	24	$R\bar{3}$	15

In rock-salt order, the crystal symmetries of double perovskites are reduced compared to their corresponding single perovskites due to the difference of B ions. For example, the $Pm\bar{3}m$ symmetry of single perovskite is reduced to $Fm\bar{3}m$ symmetry in double perovskites, as shown in Table 3. A literature survey[33] showed that, the same four kinds of Glazer tilt seen in single perovskite also dominate in double perovskites. The corresponding crystal symmetries of dominating single and double perovskite phases are shown in Table 3 with their crystal structures shown in Figure 1.

2.1.3 Perovskite Derivatives – One- and Two-Dimensional Structures

Although the octahedral tilting can break the centrosymmetry, which is critical for ferroelectricity, its effects on energy conversion process are still unclear. Recent calculations of electronic structures[19] on five common tilted phases of eighteen oxide double perovskites showed that the bandgaps resulting from different tilts can vary by up to 0.2 eV, which is slightly larger than those found in organic-inorganic halide perovskites, for example $CH_3NH_3PbI_3$[38].

When the distortion is large enough, some of the B-O bonds and therefore the three-dimensional (3D) [B-O] framework can break, resulting in one-dimensional (1D) and two-dimensional (2D) perovskite derivatives, which can be considered as low-dimensional perovskites as classified by the spatial arrangements of the octahedral units with their crystal structures depicted in Figure 1. In 1D perovskites, the [BO_6] octahedra can be corner-sharing, edge-sharing, or face-sharing to form a 1D nanowire with linear or zigzag configuration[39]. 2D perovskites typically consist of stacked layers with mainly edge-sharing octahedra[40]. These low dimensional perovskite derivatives have much higher surface to bulk ratios than their 3D counterparts, therefore, are more suitable for applications in catalysis.

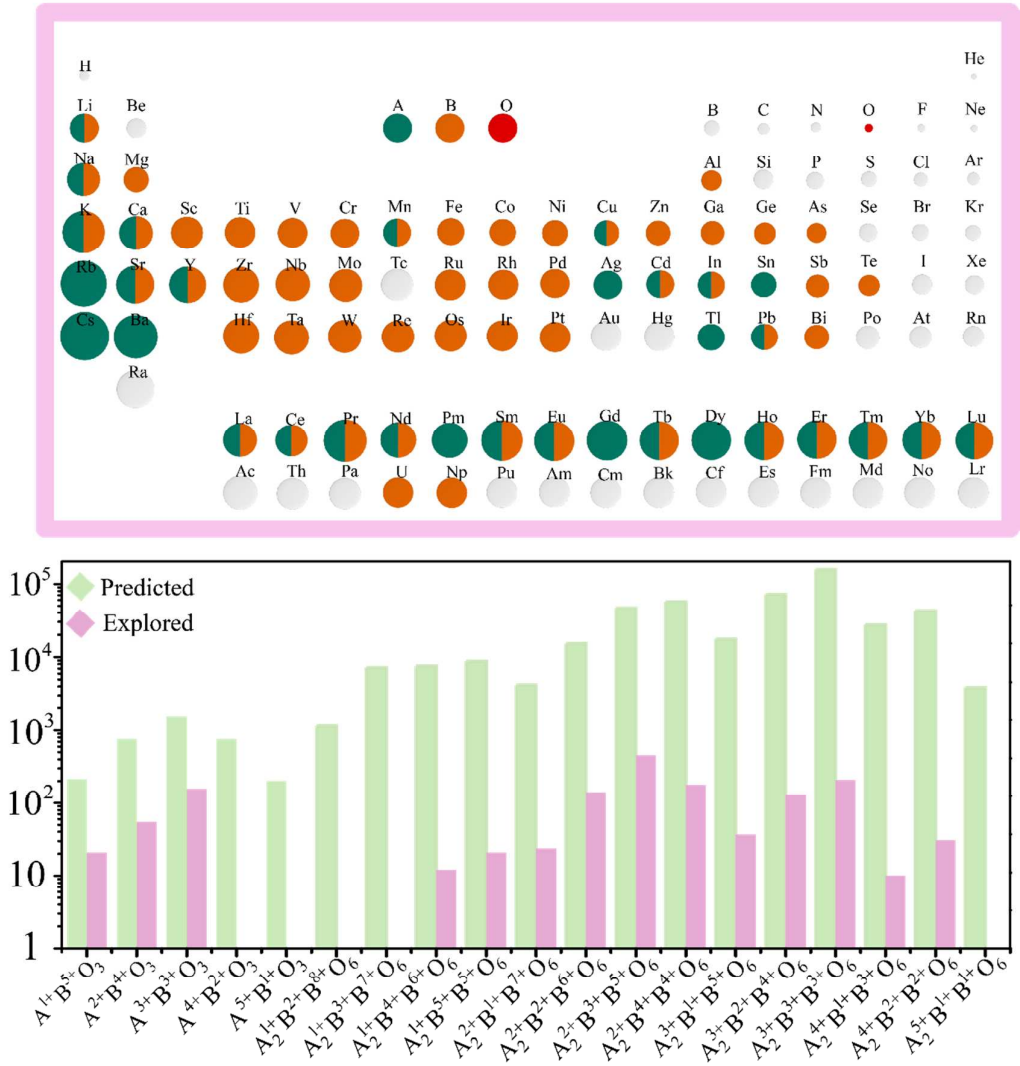

Fig. 2 Compositional flexibility of single and double oxide perovskite. A- and B-site cations are marked according to the existing single and double oxide perovskites. The bottom figure shows the ideal amount (green bar) and experimentally synthesized amount (pink bar) of oxide perovskites categorized by difference combinations of cation oxidation states. The considered oxidation states ranging from 1+ to 8+ are listed in Table 4.

2.2 Compositional flexibility

2.2.1 Stoichiometric Single Perovskites

Although perovskite was originally named for $CaTiO_3$, it was found that many different cations with diverse oxidation states and steric sizes can have similar crystal structures. Figure 2 highlights all the elements in the periodic table that have appeared on A or B site in oxide perovskites available in experimental data. There are 32/54 kinds of elements that have been found at A/B site with diverse oxidation states ranging from 1+ to 7+ and a wide range of ionic radius of 0.76 Å (Li^{1+}) – 1.52 Å (K^{1+}) for A and 0.45 Å (Be^{2+}) – 1.52 Å (K^{1+}) for B, exhibiting large flexibility of compositions that can form the crystal structure of perovskites.

In principle, the single perovskite ABO_3 can be divided into five groups, $A^{1+}B^{5+}O_3$, $A^{2+}B^{4+}O_3$, $A^{3+}B^{3+}O_3$, $A^{4+}B^{2+}O_3$ and $A^{5+}B^{1+}O_3$, according to different combinations of oxidation states of A and B cations. All cations with possible oxidation state ranging from 1+ to 8+ are listed in Table 4. In theory, there are 2346 kinds of ABO_3 and at least 265 of them have been experimentally

synthesized. Their respective numbers in each group are shown in Figure 2. There are still a large number of single perovskites that have not been expereimentally syntheised.

Tab. 4 Possible cations in periodic table with valence state from 1+ to 8+.

Note: 1. Data extracted from http://abulafia.mt.ic.ac.uk/shannon/radius.php; 2. Elements with underline are artificial, radioactive or non-metallic.

Valence	Elements																
1+	Li^{1+}	Na^{1+}	K^{1+}	Rb^{1+}	Cs^{1+}	Cu^{1+}	Ag^{1+}	Au^{1+}	In^{1+}	Tl^{1+}	Hg^{1+}	Pd^{1+}					
2+	Ag^{2+}	Am^{2+}	Ba^{2+}	Be^{2+}	Ca^{2+}	Cd^{2+}	Co^{2+}	Fe^{2+}	Cr^{2+}	Cu^{2+}	Dy^{2+}	Eu^{2+}	Sr^{2+}	Sn^{2+}	Ti^{2+}	Mg^{2+}	Tm^{2+}
	Ge^{2+}	Hg^{2+}	Mn^{2+}	Nd^{2+}	Ni^{2+}	No^{2+}	Np^{2+}	Pb^{2+}	Pd^{2+}	Pt^{2+}	Ra^{2+}	Sm^{2+}	V^{2+}	Yb^{2+}	Zn^{2+}		
3+	As^{3+}	B^{3+}	Br^{3+}	Cf^{3+}	Cm^{3+}	N^{3+}	Np^{3+}	P^{3+}	Pa^{3+}	Pd^{3+}	U^{3+}	Sc^{3+}	Mo^{3+}	Mn^{3+}	Fe^{3+}	Co^{3+}	Ni^{3+}
	Y^{3+}	La^{3+}	Ti^{3+}	V^{3+}	Nb^{3+}	Ta^{3+}	Cr^{3+}	Sb^{3+}	Bi^{3+}	Ru^{3+}	Rh^{3+}	Ir^{3+}	Sm^{3+}	Eu^{3+}	Gd^{3+}	Tb^{3+}	Lu^{3+}
	Cu^{3+}	Ag^{3+}	Au^{3+}	Al^{3+}	Ga^{3+}	In^{3+}	Tl^{3+}	Ho^{3+}	Er^{3+}	Tm^{3+}	Yb^{3+}	Dy^{3+}	Pr^{3+}	Nd^{3+}	Pm^{3+}	Bk^{3+}	Ce^{3+}
	Ac^{3+}	Pu^{3+}	Am^{3+}														
4+	Am^{4+}	Bk^{4+}	C^{4+}	Ce^{4+}	Cf^{4+}	Cm^{4+}	Co^{4+}	Cr^{4+}	Fe^{4+}	Ge^{4+}	Hf^{4+}	Ir^{4+}	Pb^{4+}	Pd^{4+}	Po^{4+}	Pr^{4+}	Pt^{4+}
	Mn^{4+}	Mo^{4+}	Nb^{4+}	Ni^{4+}	Np^{4+}	Os^{4+}	Pa^{4+}	Ti^{4+}	U^{4+}	V^{4+}	W^{4+}	Zr^{4+}	Ta^{4+}	Tb^{4+}	Tc^{4+}	Te^{4+}	Th^{4+}
	Pu^{4+}	Re^{4+}	Rh^{4+}	Ru^{4+}	S^{4+}	Se^{4+}	Si^{4+}	Sn^{4+}									
5+	As^{5+}	Au^{5+}	Bi^{5+}	Br^{5+}	Cl^{5+}	Cr^{5+}	I^{5+}	Ir^{5+}	Mn^{5+}	Mo^{5+}	N^{5+}	Nb^{5+}	Rh^{5+}	Ru^{5+}	Sb^{5+}	Ta^{5+}	Tc^{5+}
	Np^{5+}	Os^{5+}	P^{5+}	Pa^{5+}	Pt^{5+}	Pu^{5+}	Re^{5+}	U^{5+}	V^{5+}	W^{5+}							
6+	Cr^{6+}	Fe^{6+}	Mn^{6+}	Mo^{6+}	Np^{6+}	Os^{6+}	Po^{6+}	Pu^{6+}	Re^{6+}	S^{6+}	Se^{6+}	Te^{6+}	U^{6+}	W^{6+}	Ir^{6+}		
7+	At^{7+}	Br^{7+}	Cl^{7+}	F^{7+}	I^{7+}	Mn^{7+}	Np^{7+}	Os^{7+}	Re^{7+}	Ru^{7+}	Tc^{7+}						
8+	Os^{8+}	Ru^{8+}	Xe^{8+}														

2.2.2 Stoichiometric Double Perovskites

An important feature of double perovskites $A_2B'B''O_6$ is that the structure has extremely large tolerance to different elemental combinations of (B′, B″). To maintain the charge balance, $A_2B'B''O_6$ must satisfy the following equation:

$$2 \bullet Q_A + Q_{B'} + Q_{B''} = 12 \qquad (1)$$

Based on Figure 2 and Table 4, there are about 10^5 double perovskite candidates. A survey of the literature on double perovskites shows that there are more than 10^3 double perovskites being experimentally synthesized since 1950s[32, 33, 41]. Such a large number of double perovskites, with many of them have not been extensively studied yet as shown in Figure 2, provides a treasure trove of materials for wide applications.

Tab. 5 The perovskite alloys used in EC, PC, and PV.

Alloy compounds	Tolerance factor	Applications	References
$Ba_{0.5}Sr_{0.5}Co_{0.8}Fe_{0.2}O_{3-\delta}$	1.066	ORR and OER	42
$La_{1-x}Sr_xCoO_{3-\delta}$ (0,0.2,0.4,0.8,1)	1.033 (x=0.8)	ORR and OER	43
$La_{0.5}Sr_{0.5}Co_{0.8}Fe_{0.2}O_3$	1.016	ORR and OER	44
$La_{0.3}(Ba_{0.5}Sr_{0.5})_{0.7}Co_{0.8}Fe_{0.2}O_3$	1.045	ORR and OER	45
$SrNb_{0.1}Co_{0.7}Fe_{0.2}O_3$	1.027	OER	46
$SrSc_{0.025}Nb_{0.025}Co_{0.95}O_{3-\delta}$	1.036	OER	47
$La_x(Ba_{0.5}Sr_{0.5})_{1-x}Co_{0.8}Fe_{0.2}O_{3-\delta}$	1.018 (x=0.7)	ORR and OER	48
$(Pr_{0.5}Ba_{0.5})CoO_3$	1.043	OER	49

$(Sm_{0.5}Ba_{0.5})CoO_3$	1.031	OER	49
$(Gd_{0.5}Ba_{0.5})CoO_3$	1.029	OER	49
$(Ho_{0.5}Ba_{0.5})CoO_3$	1.020	OER	49
$La_{0.58}Sr_{0.4}Co_{0.4}Fe_{0.6}O_3$	1.002	ORR and OER	50
$La_{0.38}Sr_{0.6}Co_{0.2}Fe_{0.8}O_3$	1.003	ORR and OER	50
$La_{0.58}Sr_{0.4}Co_{0.6}Fe_{0.4}O_3$	1.007	ORR and OER	50
$La_{0.58}Sr_{0.4}Co_{0.8}Fe_{0.2}O_3$	1.013	ORR and OER	50
$La_{0.58}Sr_{0.4}Co_{0.2}Fe_{0.8}O_3$	0.996	ORR and OER	50
$Ca_{0.6}La_{0.4}Al_{0.4}Mn_{0.6}O_3$	1.006	ORR	51
$Ca_{0.7}La_{0.3}Al_{0.3}Mn_{0.7}O_3$	1.005	ORR	51
$Ca_{0.8}La_{0.2}Al_{0.2}Mn_{0.8}O_3$	1.005	ORR	51
$Ca_{0.9}La_{0.1}Al_{0.1}Mn_{0.9}O_3$	1.005	ORR	51
$LaNi_{0.25}Co_{0.75}O_3$	1.002	OER	52
$La_{0.8}Sr_{0.2}Mn_{0.6}Ni_{0.4}O_3$	1.002	OER	53
$La_{0.6}Sr_{0.4}Mn_{0.2}Ni_{0.8}O_3$	1.021	ORR and OER	54
$Ca_{0.9}Yb_{0.1}MnO_3$	0.997	OER	55
$La_{0.4}Sr_{0.6}CoO_3$	1.026	OER	56
$NdBa_{0.25}Sr_{0.75}Co_2O_{5+\delta}$	1.018	ORR	57
$Ca_2Mn_2O_5$	1.004	OER	58
$Ba_{0.9}Co_{0.5}Fe_{0.4}Nb_{0.1}O_3$	1.082	ORR and OER	59
$La_{0.8}Sr_{0.2}MnO_3$	0.997	ORR	60
$LaNi_{0.8}Fe_{0.2}O_3$	0.992	ORR and OER	61
$PrBa_{0.25}Sr_{0.75}Co_2O_{5.95}$	1.020	ORR and OER	62
$La(Co_{0.55}Mn_{0.45})_{0.99}O_3$	0.995	ORR and OER	63
$La_xSr_{1-x}Fe_yCo_{1-y}O_3$ (x = 0.8, 0.6, 0.4 and 0.2; y = 0.1, 0.2, 0.4, 0.6 and 0.8)	0.992 – 1.027	OER	64
$Pb(Zr,Ti)O_3$	0.991	PV	65
$(Pb,La)TiO_3$	0.996	PV	24
$(Pb,La)(Zr,Ti)O_3$	0.970	PV	24
$SrCo_{0.9}Ti_{0.1}O_3$	1.037	OER	66
$PrBa_{0.5}Sr_{0.5}Co_{1.5}Fe_{0.5}O_5$	1.020	OER	67
$LaNi_{0.85}Mg_{0.15}O_3$	0.986	ORR and OER	68
$LaTi_{0.65}Fe_{0.35}O_{3-\delta}$	0.955	ORR and OER	69
$Ba_2Bi_{1.4}Nb_{0.6}O_6$	0.942	OER and HER	21,23
Ba_2BiBiO_6	0.928	HER	23
Bi_2FeCrO_6	0.948	PV and HER	70,71
$CaCu_3Fe_4O_{12}$	0.875	OER	72
$CaCu_3Ti_4O_{12}$	0.866	Non PEC PC	73
$Ba_2Bi_{0.1}Sc_{0.2}Co_{1.7}O_6$	1.084	OER	74
$[KNbO_3]_{1-x}[BaNi_{0.5}Nb_{0.5}O_{3-\delta}]_x$	1.055 (x=0.1)	PV	22

2.2.3 Perovskite derivatives

The compositional flexibility of 3D perovskites can also be carried to 2D and 1D derivatives.

Different cations may occupy B site (octahedral center) to engineer 1D and 2D perovskites. For example, part of Ni ions in layered double hydroxides (LDHs), $Ni(OH)_2$, can be substituted by Fe ions yielding (Ni-Fe LDH) 2D perovskites[17, 75, 76] with the same 2D structure of $Ni(OH)_2$.

2.2.4 Beyond chemical stoicheometry

The compositional flexibility of perovskites is also reflected by its ease of alloying on both A and B sites. Table 5 lists part of perovskite alloys reported in recent literature for the applications in EC, PC and PV. It has been observed that the alloy site can be on either A or B site or both. For normal alloys in semiconductors, the mixing elements are usually isovalent, such as $CuIn_xGa_{1-x}Se_2$ and $Cu_2ZnSnS_{4-x}Se_x$. In contrast, mixing elements in perovskite can be nonisovalent, for example, $(La_{1.8}Ca_{0.2})(Mg_{0.9}Ti_{1.1})O_6$, where Ca^{2+} and La^{3+} are on A site and Mg^{2+} and Ti^{4+} on B′ site. The ease of cation mixing in perovskites offers great opportunities for tuning the physical and chemical properties for desirable device applications. For example, the occupation of ionic *d* orbital on B-site can be tuned by mixing transition metal ions with different valence charges, which can be used to improve the EC for chemical reactions as to be discussed in Section 3.1.

The structural and compositional flexibility also include that the structural framework of perovskite, *i.e.* the corner-sharing $[BO_6]$ octahedra, can be maintained in the presence of a large number of ionic vacancies, including A, B and O vacancies. In the extreme case, A site can be completely unoccupied, leading to the structure of ReO_3 and WO_3. In these structures, the empty A sites have large voids that are easy to accept additional ions to form A-site-deficient perovskites AWO_3[77], such as Li_xWO_3 (x=0-0.50), Na_xWO_3 (x=0-0.11 and 0.41-0.95). Such kind of A-site-deficient perovskites have also been found in titanates, niobates and tantalates, such as $La_{2/3}TiO_3$, $Ln_{1/3}NbO_3$ and $Ln_{1/3}NbO_3$. The wide cation deficincy range of A_XWO_3 offers the potential to act as anode materials in Li-ion or Na-ion batteries[78]. Apart from A-site deficiency, perovskite structures can also accommodate high density of oxygen vacancy, as shown in Table 5. In an extreme case, one O ion could be lost in one formula unit of double perovskites to form ordered-O-vacancy perovskites such as Cs_2FeAlO_5, also called brownmillerites[79]. The high oxygen deficiency and high mobility of oxygen vacancy in perovskites such as $Sr_2Mg_{1-x}Mn_xMoO_{6-\delta}$ make them suitable as anode materials in solid-oxide fuel cells[16], which require fast oxygen diffusion for chemical reaction. In fact, many functional perovskites contain oxygen vacancies, such as ferroelectric perovskites $[KNbO_3]_{1-x}[BaNi_{1/2}Nb_{1/2}O_{3-\delta}]_x$ for photovoltaics[22] (Section 3.3) and $Ba_{0.5}Sr_{0.5}Co_{0.8}Fe_{0.2}O_{3-\delta}$ for EC in OER[42] (Section 3.1.1), although the effects of oxygen vacancies are not fully understood.

3. Applications in EC, PC, and PV

The flexibilities of perovskite structure and composition enabled versatile applications of this class of materials in energy production and storage devices. In this section, we summarize recent results of their applications in EC, PC and PV. The key materials properties required for these applications will be discussed. The structure-property-application relationship of perovskites provides guidance for future materials design to overcome current challenges.

3.1 Electrocatalysis

Catalysis is crucial for the production of most industrially important chemicals. In a fundamental aspect, catalysis is the increase in the chemical reaction rate with the existence of the

catalyst[80]. Electrocatalysis is the catalysis process aided by electricity, which can also be considered as converting electrical energy to chemical energy. Figure 3 shows the types of applications of oxide perovskites and derivatives in chemical and electrochemical reactions. The results of the state-of-the-art perovskite electrocatalysts are summarized in Table 6.

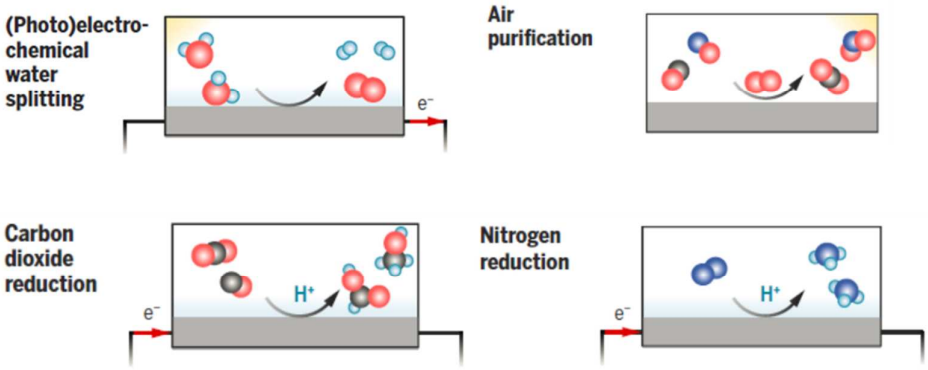

Fig. 3 Schematic pictures for chemical and electrochemical reactions involving pervoskite oxide. Reprinted with permission from Ref [81]. Copyright by the American Association for the Advancement of Science.

Tab. 6 The experimental results of oxide perovskites and derivatives for EC applications.

#, MA: Mass activities; SA: Specific activities; TOF: Turnover frequencies; *, Electrolyte: 1.0 M KOH; Others: 0.1 M KOH

Catalysts	HER (V_{RHE}@-10 mA cm^{-2})	ORR (V_{RHE}@-3mA cm^{-2})	OER (V_{RHE} @ 10 mA cm^{-2})	Intrinsic activities or Tafel slopes#	References
Single perovskite oxides					
$LaNiO_3$		0.64 V	1.66 V	89 A g^{-1}_{oxide} @1.56 V_{RHE} (MA)	82
$LaCoO_3$		0.64 V	1.64 V	100 A g^{-1}_{oxide} @1.56 V_{RHE} (MA)	83
$LaMnO_3$		0.522 V @ -1 mA cm^{-2}			84
$SrFeO_3$			1.61-1.63 V	65-70 mV dec^{-1} (Tafel slope)	85
$CaMnO_3$		0.48 V			86
Fe- and Sc-doped $SrCoO_{3-\delta}$			1.64 V	0.0065 A g^{-1}_{oxide} @1.56 V_{RHE} (MA)	87
Double perovskite oxides					
$LaNi_{0.8}Fe_{0.2}O_3$		0.61 V	1.68 V	N/A	61
$LaNi_{0.75}Fe_{0.25}O_3$		0.67 V	1.68 V	82 A g^{-1}_{oxide} @1.56 V_{RHE} (MA)	83
$La_{0.5}Sr_{0.5}CoO_{3-\delta}$		0.76 V	1.83 V	N/A	88
$La_{0.6}Sr_{0.4}CoO_{3-\delta}$		0.67 V	1.82 V	N/A	89
$La_{0.5}Sr_{0.5}Co_{0.8}Fe_{0.2}O_3$		0.63 V	1.82 V	N/A	90
$La_{0.58}Sr_{0.4}Co_{0.2}Fe_{0.8}O_3$		0.77 V	1.68 V	N/A	91
$Ba_{0.5}Sr_{0.5}Co_{0.8}Fe_{0.2}O_{3-\delta}$		0.61 V	1.73 V	129 mV dec^{-1} (Tafel slope)	92
$La_{0.3}(Ba_{0.5}Sr_{0.5})_{0.7}Co_{0.8}Fe_{0.2}O_{3-\delta}$		0.61 V	1.61 V	N/A	45
$(Pr_{0.5}Ba_{0.5})CoO_{3-\delta}$			1.57 V	60 mV dec^{-1} (Tafel slope); 1.0 mA cm^{-2}_{oxide} @1.65 V_{RHE} (SA)	49
$SrNb_{0.1}Co_{0.7}Fe_{0.2}O_{3-\delta}$	-0.232 V		1.60 V	61 mV dec^{-1} (Tafel slope)	93
$LaTi_{0.65}Fe_{0.35}O_{3-\delta}$		0.51 V			69
$LaNi_{0.8}Fe_{0.2}O_3$		0.64 V	1.74 V	N/A	61
$LaNi_{0.75}Fe_{0.25}O_3$		0.56 V			83
$PrBa_{0.5}Sr_{0.5}Co_{1.5}Fe_{0.5}O_{5+\delta}$			1.588 V	52 mV dec^{-1} (Tafel slope); 71 A g^{-1}_{oxide} (MA) and 3.8 mA cm^{-2}_{oxide} @1.60 V_{RHE} (SA)	67
$Ba_2CoMo_{0.5}Nb_{0.5}O_{6-\delta}$			1.675 V	77 mV dec^{-1} (Tafel slope); 43 A g^{-1}_{oxide} @1.67 V_{RHE} (MA)	94
$SrCo_{0.4}Fe_{0.2}W_{0.4}O_{3-\delta}$*			1.526 V	50 mV dec^{-1} (Tafel slope); 58 A g^{-1}_{oxide} (MA) and 2.1 mA cm^{-2}_{oxide} @1.64 V_{RHE} (SA)	95
P-doped $LaFeO_{3-\delta}$		0.2V @ -6.41 mA cm^{-2}	1.69 V	50 mV dec^{-1} (Tafel slope)	96
$LaCu_{0.5}Mn_{0.5}O_3$		0.6			97
$(PrBa_{0.85}Ca_{0.15})_{0.5}(MnFe)_{0.5}O_{3-\delta}$		0.68 V @ $E_{1/2}$	1.63 V	86 mV dec^{-1} (Tafel slope)	98
Derivatives					

$MnCoFeO_4$		0.78 V	1.71 V	0.011s^{-1} @1.53 V_{RHE} (TOF)	99
$La_{0.9}FeO_3$		0.38 V	1.64 V	23.56 A g^{-1}_{oxide} (MA) and 0.364 mA cm^{-2}_{oxide} @1.63 V_{RHE} (SA)	100
$Ca_2Mn_2O_5$			1.7 V	6.39 A g^{-1}_{oxide} @1.60 V_{RHE} (MA)	58
$SrCo_{0.95}P_{0.05}O_3$			1.71 V	84 mV dec^{-1} (Tafel slope)	101
$CaCu_3Fe_4O_{12}$			1.61 V	51 mV dec^{-1} (Tafel slope); ~ 8 mA cm^{-2}_{oxide} @1.60 V_{RHE} (SA)	72
$Sr_{0.95}Nb_{0.1}Co_{0.7}Fe_{0.2}O_{3-\delta}$			1.69 V	70 mV dec^{-1} (Tafel slope)	102
$LaSr_3Co_{1.5}Fe_{1.5}O_{10-\delta}$			1.62 V	83.9 mV dec^{-1} (Tafel slope);113.8 A g^{-1}_{oxide} @1.68 V_{RHE} (MA)	103
$Ba_2Bi_xSc_{0.2}Co_{1.8-x}O_{6-\delta}$			1.75 V@5.1 mA cm^{-2}	102 mV dec^{-1} (Tafel slope); 3.9 A g^{-1}_{oxide} @1.73 V_{RHE} (MA)	74
$PrBa_{0.5}Sr_{0.5}Co_{2-x}Fe_xO_{5+\delta}$		0.68 V	1.53 V	81 mV dec^{-1} (Tafel slope)	104
$NdBaMn_2O_{5.5}$	-0.29 V		1.66 V	75 mV dec^{-1} (Tafel slope); 2.06 mA cm^{-2}_{oxide} @1.70 V_{RHE} (SA)	105
$CoSn(OH)_6^*$			1.504 V	N/A	106

3.1.1 Single Perovskites

The studies on the single perovskites as oxygen electrocatalysts were firstly reported during early 1970*s*[107]. Meadwcroft examined the EC activity of several single oxide pervoskites[107]. Among them, $LaCoO_3$ showed promising performance in base and Sr or Ni doping was found to improve the conductivity to 10^2 Ω cm^{-1}. The early study of trivalent Ni-containing perovskites $LaNiO_{2.84}$ for ORR suggested the feasibility of σ* bond formation between the e_g orbital of the transition metal ion and molecular orbital of adsorbate, which is important for EC activity. In addition, the conductity of oxide perovskite is strongly correlated with the oxgen vancancies, which further affects the catalytic activities.[108] Several other 3*d*-transition metal-containing perovskite (e.g., $LaVO_3$, $LaMnO_3$, $SrFeO_3$, etc)[84, 109] have been stuided for OER/ORR in base. For instance, the ORR activties of $LnMnO_3$ (Ln = La, Pr, Nd, Sm, Gd, Dy, Yb, or Y) were studied in 8.0 M KOH with similar surface areas.[110] It was found that the activities decreased with the decrease in the ionic radius of the A-site cation (La>Pr>Nd>Sm>Gd>Y>Dy>Yb). Both the tolerance factor and symmetry increase with the the increase of A-site cation radius. Therefore, La^{3+}, with the largest ionic radius in the series, tends to form the highly symmetric cubic or rhombohedral phases, while Pr^{3+} and Nd^{3+}, with smaller ionic radius, tend to form the orthorhombic or tetragonal phases. The crystal structures are stongly correlated with the electrocatalytic acitivities, due to the distortion of the [BO_6] octahedra, and therefore also indirectly influence the ORR/OER activity[110].

Sunarso *et al.*[111] investigated the ORR activities of $LaMO_3$ (M = Cr, Mn, Fe, Co, and Ni) in 0.1 M KOH. The results indicated a descending order (Co>Mn>Ni>Fe>Cr) in diffusion-limited ORR current density. Zhu *et al.*[112] studied the EC activities of $LaMO_3$ (M = Mn, Fe, and Co) perovskite nanoparticles for both ORR and OER. $LaMnO_3$ was found to have the best bifuctional activities for both OER and ORR, followed by $LaCoO_3$ and $LaFeO_3$, whereas $LaCoO_3$ exhibited

better stability than $LaMnO_3$. Hardin *et al.*[83] examined $LaMO_3$ (M = Ni, Co, and Mn) with pure perovskite phases. The results indicate that $LaCoO_3$ has the lowest overpotential of 1.64 V_{RHE} at 10 mA cm^{-2} (OER), and 0.64 V_{RHE} at -3 mA cm^{-2} (ORR) in 0.1 M KOH. In addition, their work also suggested strong performance dependence on the formation energies of oxygen vacancy.

To further understand the mechanism, a number of descriptors have been proposed to guide new materials design. For instance, Man *et al.*[113] calculated the adsorption energies of HOO* vs. HO* to analyze the reaction free energy diagrams of OER electrocatalysts. The scaling relation led to an approximately constant difference between the binding energies of HOO* and HO*, which in turn defined the lowest possible theoretical overpotential for the OER on a wide variety of oxides. Based on that, they introduced a single descriptor ($\Delta G_{O*} - \Delta G_{HO*}$) to evaluate the EC activity. When thermodynamic overpotentials are plotted with this descriptor, a volcano plot was obtained. The oxide on the very top of the volcano shows better performance than its beneath counterparts (Figure 4), and two different slopes indicate two different rate-determining steps. Oxides on the left-hand branch mean too strong binding with adsorates, while oxides on the right-hand branch indicate too weak bindings. This behavior is typically referred as to the Sabatier principle. Although the Sabatier principle can well explain the activity trend of oxide perovskite, it is difficult to perdict novel catalysts with enhanced activity. In addition, the proposed mechanism using this descriptor is based on four-electron reaction paths, and the actual reaction path may differ.

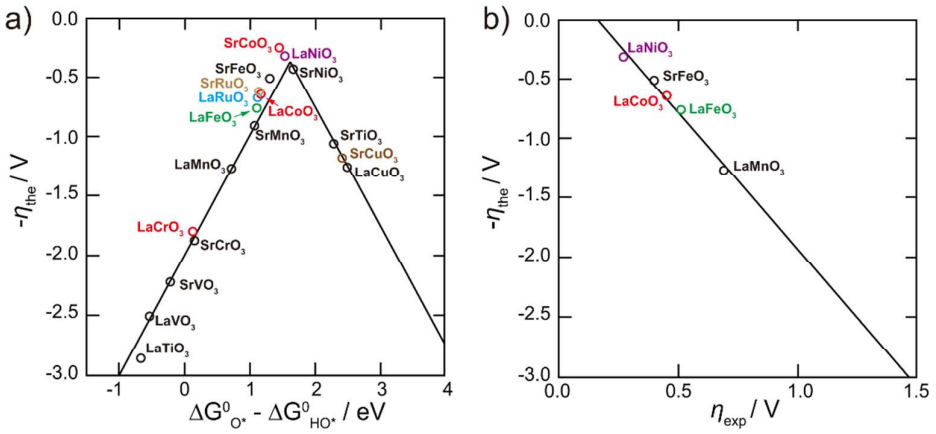

Fig. 4 a) Activity trends towards oxygen evolution plotted for perovskites.The negative theoretical overpotential was plotted against the standard freeenergy of the $\Delta G^0_{O*} - \Delta G^0_{HO*}$ step. The low coverage regime was considered and the calculated values were used to show the activity of each oxide. The volcano curve was established by using the scaling relation between $G^0_{HOO*} - G^0_{O*}$ and $G^0_{O*} - G^0_{HO*}$. b) Theoretical overpotential vs the experimental overpotential in alkaline media. All experimental values were recorded at 10 mA cm^{-2}, room temperature, and pH 14. Reprinted with permission from ref [113]. Copyright 2011, Wiley-VCH Verlag GmbH & Co. KGaA, Weinheim.

3.1.2 Double Perovskites

In order to tune effective e_g orbital, Co, Fe and V were introduced into $LaNiO_3$ to partially substitute Ni in early 1970*s*, leading to double perovskite electrocatalysts.[108] The results indicated that the overlap integral of e_g and O 2*p* orbital was the descriptor of EC activity. The larger overlap integral corresponds to higher the EC activity. Other 3*d*-transition metal-containing double perovskites were reported for oxygen electrocatalysis by partially replacing B-site cations. For instance, a systematic examinations of 14 perovskites for OER revealed a descending order: $La_{0.58}Sr_{0.4}Co_{0.2}Fe_{0.8}O_3$ > $La_{0.76}Sr_{0.2}Co_{0.2}Fe_{0.8}O_3$ > $La_{0.83}Ca_{0.15}Mn_{0.6}Co_{0.4}O_3$ > $La_{0.6}Sr_{0.4}FeO_3$ >

$La_{0.74}Sr_{0.2}Co_{0.2}Fe_{0.8}O_3$ > $La_{0.58}Sr_{0.4}Co_{0.2}Cu_{0.1}Fe_{0.7}O_3$ > $La_{0.75}Sr_{0.2}Mn_{0.9}Co_{0.1}O_3$ > $La_{0.97}Mn_{0.4}Co_{0.3}Cu_{0.3}O_3$, while $Pr_{0.65}Sr_{0.3}MnO_3$, $La_{0.78}Sr_{0.2}Co_{0.2}Fe_{0.8}O_3$, $La_{0.7}Sr_{0.25}Mn_{0.5}Cr_{0.5}O_3$, $La_{0.78}Sr_{0.2}FeO_3$, $La_{0.58}Sr_{0.4}FeO_3$, and $La_{0.65}Sr_{0.3}MnO_3$ showed negligible catalytic activity toward OER.[114] The results suggest that the OER performance is sensitive to cations and minor variations in stoichiometry. Sunarso *et al.*[111] investigated the ORR activities of double perovskite $LaNi_{0.5}M_{0.5}O_3$ (M = Cr, Mn, Fe, Co, and Ni) in alkaline solution. It was found that Mn-doping demonstrated the best performance based on ORR-limited current densities.[111] Later, Yuasa *et al.*[115] confirmed the observations by investigating the ORR activities of $La_{0.4}Ca_{0.6}Mn_{1-y}Fe_yO_3$ by tuning the Fe content. Their results indicated that a higher Mn content rather than a higher Fe content leads in higher activities on both ORR-limited current densities and onset potentials. Precious metals are also investigated as substitution cations (e.g., $La_{0.6}Ca_{0.4}Co_{0.8}Ru_{0.2}O_3$) for improving the activities for oxygen electrocatalyst.

Different from B-site cations, A-site cations usually do not contribute to the electronic structure near the Fermi level. However, they may affect valence state of B-site ions, electronic conductivities, crystal structures, electrochemically active area, and oxygen vancancies. In late 1970*s*, Obayashi *et al.*[116] studied the $LnMM'O_3$ (Ln: lathanoid, M: alkaline earth, M': transition metal) perovskite oxides as oxygen electrocatalysts, and they found that Sr substitution showed the best result and $La_{1-x}Sr_xCoO_3$ and $La_{1-x}Sr_xNiO_3$ showed the highest activities among all of the studied pervoskites. The results were also confirmed by Tiwari *et al.*[117]. $La_{1-x}Sr_xCoO_3$ showed two Tafel slopes: 57 to 64 mV dec^{-1} at low and 100 to 130 mV mV dec^{-1} at high overpotentials. They also found that Sr substitution dramatically enhanced the electrochemically active area. Another studies on the subsitutions of A-site cations Ca by lanthanide (La, Nd, Sm, Gd, Y and Ho) in $CaMnO_{3-\delta}$ showed that La^{3+} substitution resulted in enhancements in both electronic conductivity and porosity.[118] The enhanced conductivity may be related to the absence of 4*f* electrons of La^{3+} and the oxygen vancancies.

Perovskites with both A- and B-site cations substitutions ($A_{1-x}A'_xB_{1-y}B'_yO_{3-\delta}$) were also intensively studied. For instance, Azizi *et al.*[119] investigated $Sr_{1.5}La_{0.5}FeMoO_6$ for bifuctional OER and ORR. The results showed superior activities resulting from enhanced electrical conductivity. Among all of these perovskites, $Ba_{0.5}Sr_{0.5}Co_{0.8}Fe_{0.2}O_{3-\delta}$ (BSCF), has received speical attentions.[120] BSCF possessed high intrinsic OER activity (oxide surface area normalized current density), which was measured to be at least 1 order of magnitude higher than that of the state-of-the-art catalyst (IrO_2 nanoparticles, ~6 nm) in alkaline solution at the same potential.[42] Early studies suggested that the high activities can be attributed to high electronic and ionic conductivity, high concentration of oxygen vacancies and high oxygen exchange kinetics.[121-123] In 2011, Suntivich *et al.* demonstrated a volcano-like trend for OER activity versus e_g orbital filling.[42] This study systematically evaluated more than 10 perovskites, where double perovskites BSCF with an e_g filling close to 1, occupied the peak (Figure 5). As discussed above, e_g orbital at perovskite surface will interact with the absorbates in the electrolytes through σ bonding[81]. Thus, the e_g occupancy will strongly affects the bonding length/energy and thus the OER performance. Since the e_g orbital is antibonding, a high e_g occupation corresponds to a weak bonding, and a low occupation corresponds to a strong bonding. Therefore, an e_g occupancy of approximately 1 produces the highest activity according to the Sabtier principle, as observed in BSCF.

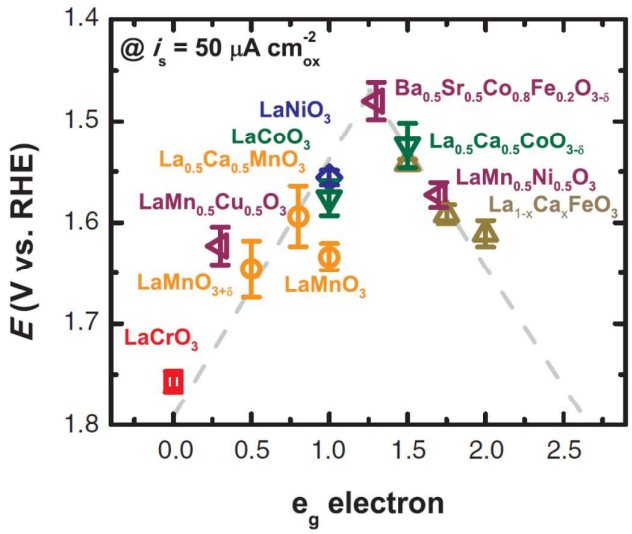

Fig. 5 The relation between the OER catalytic activity, defined by the overpotentials at 50 mA cm_{ox}^{-2} of OER current, and the occupancy of the e_g-orbital of the transition metal B. Data symbols vary with type of B ions (Cr, red; Mn, orange; Fe, beige; Co, green; Ni, blue; mixed compounds, purple), where x = 0, 0.25, and 0.5 for Fe. Error bars represent SDs of at least three independent measurements. Reprinted with permission from ref [42]. Copyright 2011 by the American Association for the Advancement of Science.

In 2013, Grimaud *et al.*[49] synthesized a new group of double perovskites, $Ln_{0.5}Ba_{0.5}CoO_{3-\delta}$ (Ln = Pr, Sm, Gd, Ho and Ln). Their intrinsic OER activities, normalized to surface areas, are comparable to BSCF, which is 1 order of magnitude higher than that of $LaCoO_3$. In comparison to BSCF, which readily amorphizes during the oxygen evolution reaction, $Ln_{0.5}Ba_{0.5}CoO_{3-\delta}$ showed no significant changes during cycling, indicating the high stability. The high activity and stability of these double perovskites were explained by having the O *p*-band centre neither too close nor too far from the Fermi level, which was computed from *ab initio* studies[49]. This mechanism is illustrated in Figure 6. Similar observations have been found for ORR. A stronger covalency of the B–O bond should increase the driving force and thereby facilitate the O^{2-}/OH^- exchange on the surface B ions, which can be considered as the rate-limiting step of ORR.

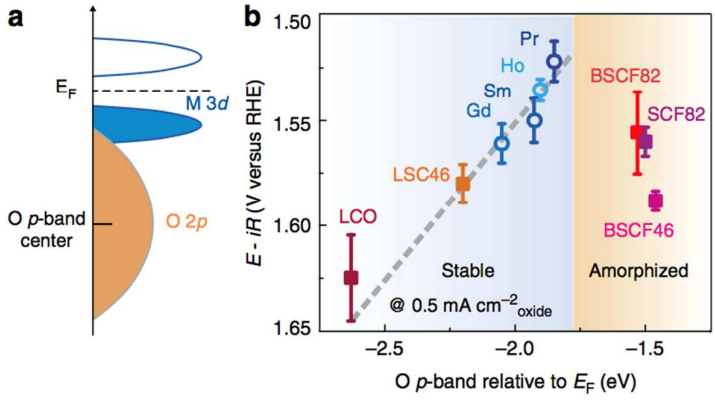

Fig. 6 Computed O p-band center for oxygen evolution. (a) Schematic representation of the O p-band for transition metal oxides and (b) evolution of the iR-corrected potential at 0.5 mA cm^{-2}_{oxide} versus the O p-band center relative to E_F (eV) of $(Ln_{0.5}Ba_{0.5})CoO_{3-\delta}$ with Ln = Pr, Sm, Gd and Ho, for $LaCoO_3$ (LCO), $La_{0.4}Sr_{0.6}CoO_3$ (LSC46), $Ba_{0.5}Sr_{0.5}Co_{0.8}Fe_{0.2}O_{3-\delta}$ (BSCF82), $Ba_{0.5}Sr_{0.5}Co_{0.4}Fe_{0.6}O_{3-\delta}$ (BSCF46) and $SrCo_{0.8}Fe_{0.2}O_{3-\delta}$ (SCF82). Error bars represent s.d. from at least four independent measurements. Reprinted with permission from ref [49]. Copyright 2013 Nature Publishing Group.

In 1980*s*, oxide perovskites have been examined as catalysts for the synthesis of chemical fuels from CO.[124] Broussard *et al.*[125] found that $LaMnO_3$ can catalyze the reduction of CO by hydrogen to hydrocarbons with 100% selectivity, and double perovskite $LaMn_{0.5}Cu_{0.5}O_3$ leads to high selectivity to methanol. Cu^0 and Cu^{n+} are believed to be the key factor for production of alcohols, while pristine Cu^0 only yeilds hydrocarbons. Similar findings were also obtained for $LaRhO_3$, where methane was formed over Rh metal and oxygenates (up to 80 % by weight) were produced over $LaRhO_3$.[126] Later, Schwartz *et al.* studied the electrochemical CO_2 reduction to alcohols on $La_{1.8}Sr_{0.2}CuO_4$, and found a Faradaic efficiency up to 40 % at a current density of 180 mA cm^{-2}.[127]

3.1.3 Non-stoichiometric Perovskites and Derivatives

It was proposed that the electronegativity, which tended to increase in late 3*d* elements with high oxidation states, was responsible for increasing the metal–oxygen covalency.[72] In this regard, a perovskite containing high-spin Fe^{4+} ions, $CaCu_3Fe_4O_{12}$ has been synthesized, which showed high activity, comparable to or exceeding those of the state-of-the-art catalysts such as BSCF and RuO_2. In addition, the substitution of "A" site with transition metals may form a covalent bonding network, which prevents the leaching of alkaline earth metal. As a result, a higher stability was achieved associated with greatly reduced thickness of amorphous layers on the surface of catalysts.[72]

Kim *et al.* synthesized an oxygen-deficient perovskite electrocatalyst, $Ca_2Mn_2O_5$, through a reductive annealing method for OER in alkaline media. The catalyst showed an onset potential of 1.50 V_{RHE}, and reached an OER mass activity of 30.1 A g^{-1} at 1.70 V_{RHE}. The results suggest that the oxygen vacancies and high spin electron configuration on Mn are likely contributing to the enhanced performance.[58] Jung *et al.* reported Sr^{2+} or Ca^{2+} doped La_2NiO_4 as bifunctional catalysts for OER and ORR[128]. Sr-doping showed the highest OER and ORR acitivities. The increased Sr substitution likely drived the Ni oxidation state to be closer to 3+, corresponding to an e_g-filling of approximately 1.

"A" site cations extraction or partially substitution is proven to be an effective method for enhancing the metal-oxygen covalency to achieve higher OER activities. This is because partial substitution on A-site by low-valence metal ions generates additional oxygen vacancies and shifts a large proportion of the B-site transition-metal ions to unstable oxidation states (B^{3+}/B^{4+} redox couple).[129, 130] This may result in enhanced oxygen mobility and kinetics, thereby increased EC activities. For instance, our previous report on the O3-type metaloxides, $NaNi_{0.9}Fe_{0.1}O_2$, demonstrated that the extraction of Na can lead to the improvements on OER activity, which correlated to the enhancement of valence states of Ni.[17] Similarly, Seitz *et al.*[131] reported that the Sr leaching from surface layers of thin films of perovskite $SrIrO_3$ generated highly active surface layers with IrO_3 or anatase IrO_2 motifs. As a result, the $IrO_x/SrIrO_3$ catalyst outperformed IrO_x and ruthenium oxide (RuO_x) systems. It achieved 10 mA cm^{-2} at 270 mV overpotential for 30 h of continuous testing in acidic electrolyte.

Recently, layered $Ni_{0.9}Fe_{0.1}OOH$ was found to be an active catalyst in a study of the in-situ structure transformation from $Ni_{0.9}Fe_{0.1}O_x$, which is in direct parallel with the increasing catalytic activity.[132] The layered structure allows the intercalation of water and anions, leading to high bulk redox activity.[133] Studies on ZnCo layered double hydroxide (LDH) further confirmed that catalysts with such a layered structure had higher activities than Co-based catalysts with other

structures.[134] Gong *et al.*[75] reported that incorporation of Fe into the nickel hydroxide induced the formation of NiFe-LDH. The crystalline NiFe-LDH phase in nanoplate form is found to be highly active for OER in alkaline solutions. Driving by halide perovskite solar cells, the NiFe-LDH catalyst was able to reach a solar-to-hydrogen conversion efficiency of 12.3% for splitting water,[135] owning to its excellent OER and HER activities (as indicated in Figure 7). Although 2D structure provides much higher active surface for catalysis reaction, the weak interactions between layers hinder charge collection and transportation. Synthesizing ultrathin NiFe-LDH nanoplates on mildly oxidized multiwalled carbon nanotubes (CNTs) has been used to improve the charge transportations[75]. A NiFe-LDH/CNT complex exhibited higher EC activity and stability for OER than commercial precious metal Ir catalysts. Long *et al.*[76] used graphene to further enhance the electron transport, resulting in superior electrocatalytic properties of the FeNi-GO hybrids for OER with overpotentials as low as 0.21 V, which was further reduced to 0.195 V after the reduction treatment (FeNi-rGO).

Increasing the oxidation states of Ni is a viable approach to further improve the OER activity of FeNi-LDH. Unfortunately, increasing the oxidation states of layered FeNi-LDH is very hard due to the formation of metaphases.[42, 75, 76] Weng *et al.*[17] synthesized $NaNi_yFe_{1-y}O_2$ with Na intercalated in layered $Ni_yFe_{1-y}O_2$ and then reduce the Na content by chemical extraction of Na, forming $Na_{1-x}Ni_yFe_{1-y}O_2$, which is a layered double oxide consisting of $[MO_6]$ (M = Ni, Fe) octahedral layers with some residual Na atoms lying between the octahedral layers. Like NiFe-LDH, the layered $Na_{1-x}Ni_yFe_{1-y}O_2$ double oxide structure provides more active sites than the O3 phase. The use and extraction of Na enforce Ni and Fe to high chemical states. As a result, the new $Na_{1-x}Ni_yFe_{1-y}O_2$ electrocatalysts exhibited remarkable OER activity and excellent stability. The same strategy can be applied to synthesize efficient $Na_{1-x}Co_{1-y}Fe_yO_2$ OER catalysts. The superior catalytic properties can be ascribed to the layered structure as well as the enhanced covalency of Ni and Fe.

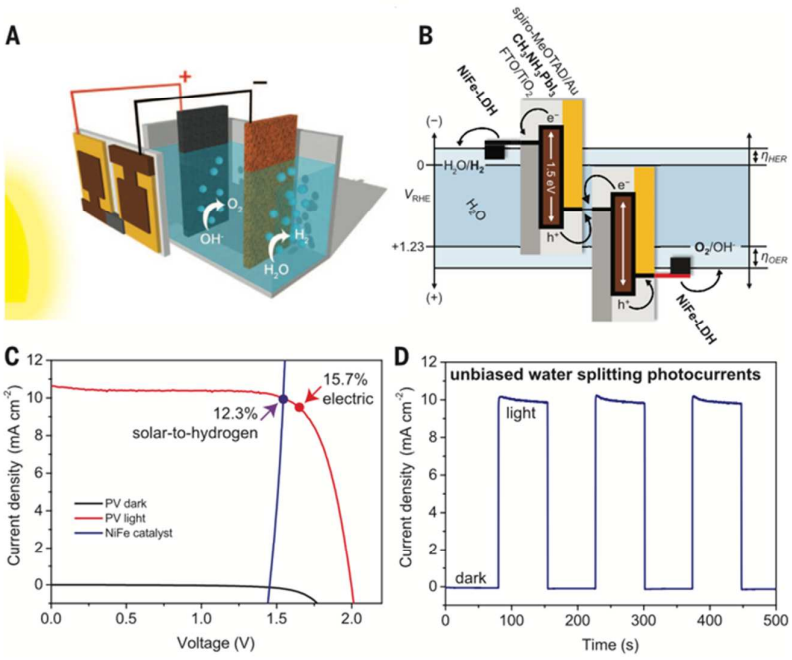

Fig. 7 Combination of the perovskite tandem cell with NiFe DLH/Ni foam electrodes for water splitting. (A) Schematic diagram of the water-splitting device. (B) A generalized energy schematic of the perovskite tandem cell

for water splitting. (C) J–V curves of the perovskite tandem cell under dark and simulated AM 1.5G 100 mW cm^{-2} illumination, and the NiFe/Ni foam electrodes in a two-electrode configuration. The illuminated surface area of the perovskite cell was 0.318 cm^2, and the catalyst electrode areas (geometric) were ~5 cm^2 each. (D) Current density–time curve of the integrated water- splitting device without external bias under chopped simulated AM 1.5G 100 mW cm^{-2} illumination. Reprinted with permission from ref [135]. Copyright 2014 by the American Association for the Advancement of Science.

3.2 Photocatalysis

In PC devices, electrocatalysts are deposited onto solar absorber materials and the whole device is immersed into electrolyte. The electrodes usually play both roles of sunlight absorber and electrocatalyst. Therefore, the materials for photoelectrodes should satisfy stringent conditions in terms of stability under operating conditions, light absorption in the visible range, adequate alignment of band edges with the relevant redox potentials and overall efficiency.[1, 5, 7, 136-153] In a non-PEC PC device, both the oxidation and reduction reactions take place on the same photoelectrode. The reaction production rates are used to characterize the efficiency of the device. In a PEC PC device, oxidation reaction occurs on the anode, whereas the reduction reaction happens on the cathode. The photocurrent is more often used than production rates to characterize the device efficiency. Oxide perovskites have been intensively studied for photocatalytic water splitting (both non-PEC and PEC) for hydrogen production (partially listed in Table 7). Recently, oxide perovskite-based photocatalytic CO_2 reduction is now emerging as an important direction for solar-to-fuel conversions.

3.2.1 Single Perovskites

As a typical perovskite, $SrTiO_3$ (STO) has been studied for photocatalyzing the overall water splitting and CO_2 reduction. STO has a large band gap of 3.2 eV, and its bulk form can split water into stoichiometric mixtures of H_2 and O_2. A hydrogen production rate of 28 μmol H_2 g^{-1} h^{-1} was reported when NiO was used as the cocatalyst.[157] It was also found that decreasing the particle size reduced the hydrogen production rate. For instance, STO with particle size of 30 ± 5 nm (6.5 ± 1 nm) delivered hydrogen with the rate of 19.4 μmol H_2 g^{-1} h^{-1} (3.0 μmol H_2 g^{-1} h^{-1}). The reasons for this decrease was attributed to the increase of the water oxidation overpotential and reduced light absorption due to quantum size effect for the smaller particles.[153] Shoji *et al.*[154] reported photocatalytic conversion of CO_2 to CO on the surface of STO with amorphous Cu_xO as the cocatalyst, under UV irradiations. The CO evolution rate was estimated to be 0.65 μmol $h^{-1}cm^{-2}$, with a CO selectivity of ~ 83%. The loading of Cu_xO was found to improve the CO selectivity by 20%. Bi *et al.*[155] studied the photocatalytic CO_2 reduction on TiO_2/STO heterojunction, and they found CH_4 and CO as the gaseous products. Pt and Pd loading remarkably enhanced the photo-conversion efficiency of CO_2 to CH_4, achieving the highest production rate of 20.83 ppm $h^{-1}cm^{-2}$ with Pd as the co-catalyst. Yoshida *et al.*[156] reported Ag coated $CaTiO_3$ for photocatalytic CO_2 reduction, with CO production rate up to 2.25 μmol $h^{-1}g^{-1}$ (CO selectivity up to 44%).

Beside STO, many other single perovskites have been tested for PC applications. Bulk $NaTaO_3$ with a bandgap of ~ 4.0 eV showed the ability to deliver H_2 production rate up to 36,750 $\mu mol^{-1}g^{-1}h^{-1}$, in the presence of methanol in the electrolyte.[146] Another study showed that it can produce 19,800 $\mu mol^{-1}g^{-1}h^{-1}$ of H_2 with NiO (0.02 wt%) as the catalyst.[147] Nakanishi *et al.*[157] found that Sr doped $NaTaO_3$ showed the highest CO production rate of 176 μmol h^{-1} (mass loading 0.25 to 0.5 g) with 2 wt% Ag as the cocatalyst (CO selectivity of 86%) under UV irradiations. Ca doping showed an inferior of CO production rate of 148 μmol h^{-1}, but with a

higher CO selectivity up to 91%. Bulk $LiTaO_3$, $AgTaO_3$, and $KTaO_3$ have bandgaps of 4.7, 3.4 and 3.6 eV, respectively. Kato *et al.* reported the corresponding H_2 production rates under UV illuminations of 430, 138 (with 0.3 wt% NiO as catalyst) and 29 $\mu mol^{-1}g^{-1}h^{-1}$, for these perovskites respectively.[148, 149] The niobates have smaller bandgap compared to their tantalate counterparts. For instance, $KNbO_3$, $NaNbO_3$, $AgNbO_3$, and $Sr_{1-x}NbO_3$ have bandgaps of 3.12, 3.8, 2.9 and 1.9 eV, respectively.[150-152] Hydrothermal synthesized $KNbO_3$ nanowires produced 5,170 $\mu mol^{-1}g^{-1}h^{-1}$ of H_2, under UV illumination with 25% methanol addition and 0.25 wt% Pt as catalyst.[157] $AgNbO_3$ was able to produce 5.9 $\mu mol^{-1}g^{-1}h^{-1}$ of H_2 under visible light irradiations (>420 nm) at the same conditions for $KNbO_3$.[151] $Sr_{1-x}NbO_3$ delivered 44.8 $\mu mol^{-1}g^{-1}h^{-1}$ of H_2 in the presence of oxalic acid and 5 mM $AgNO_3$ under visible light irradiations (>420 nm).[150] Titanates, such as $SrTiO_3$, $CaTiO_3$, $PbTiO_3$, usually have bandgaps between 2.8 to 3.3 eV,[153, 158-164] while ferrites such as $BiFeO_3$, $LaFeO_3$, $SrFeO_3$, $CaFeO_3$, usually have bandgap between 1.8 to 2.7 eV.[165, 166] Hydrothermal synthesized $BiFeO_3$ nanowires with a bandgap of 2.35 eV was reported to produce H_2 at a rate of 400 $\mu mol^{-1}g^{-1}h^{-1}$, in the presence of 4 mM $FeCl_3$ and under visible light illumination (>380 nm).[165] Sol-gel synthesized $LaFeO_3$ showed a superior hydrogen production rate of 8,600 $\mu mol^{-1}g^{-1}h^{-1}$ in the presence of 10% methanol without catalysts loading under visible light illumination (>420 nm).[166]

Tab. 7 The experimental results of oxide perovskites for photocatalytic water splitting.

photo-absorbers	Substitution sites	Bandgap (eV)	Incident light	Scarification reagents in the solutions	Electrocatalysts (wt%)	Activity ($\mu molg^{-1}h^{-1}$)/Gas or photocurrent density @ V_{RHE} (Non-PEC/PEC)	References
Single perovskites							
$NaTaO_3$		4.00	UV	W/O	0.05% NiO	2,180/H_2	167-169
$NaTaO_3$ (hydrothermal reacted)		3.96	UV	5% methanol	W/O	36,750/ H_2	146
La-doped $NaTaO_3$	A-site	4.09	UV	W/O	0.02% NiO	19,800 H_2	147
Ca, Sr, Ba-doped $NaTaO_3$	A-site	4.00	UV	W/O	0.1% NiO	27,200/ H_2	170
$Na_{1-x}K_xTaO_3$	A-site	3.75	UV	W/O	W/O	11,000/ H_2	171
Ta^{4+} doped $NaTaO_3$	B-site	1.70	>420nm	w/O	W/O	61/ H_2	172
Bi-doped $NaTaO_3$	B-site	2.88	> 400 nm	5% methanol	0.02% NiO	59.5/ H_2	173
$LiTaO_3$		4.70	UV	W/O	W/O	430/ H_2	149
$KTaO_3$		3.60	UV	W/O	W/O	29/ H_2	149
$AgTaO_3$		3.40	UV	W/O	0.3% NiO	138/ H_2	148
$KNbO_3$ nanowires		3.20	UV	12% methanol	0.5% Pt	5,170/ H_2	152
$AgNbO_3$		2.80	> 420 nm	20%	1% Pt	5.9/ H_2	151

				methanol			
$Sr_{1-x}NbO_3$		1.90	> 420 nm	Oxalic acid/5 mM $AgNO_3$	W/O	44.8/ H_2	150
$SrTiO_3$		3.20	UV	W/O	3.0% NiO	28/ H_2	153
Cr-doped $SrTiO_3$ nanoparticles	B-site	2.30	> 420 nm	5% methanol	1.0% Pt	330/ H_2	158
Mn-doped $SrTiO_3$	B-site	2.70	> 440 nm	10% methanol 50 mM $AgNO_3$	0.5% Pt	8.9/O_2 (0.66/ H_2)	159
Zn-doped $SrTiO_3$	B-site	3.15	UV	3% methanol	W/O	732/ H_2	160
Ti^{3+} doped $SrTiO_3$	B-site	3.20	UV	25% methanol	1.0% Pt	2,200/ H_2	161
Cu-doped $CaTiO_3$	B-site	N/A	> 400 nm	W/O	NiO_x	22.7/ H_2	162
$CaTiO_3$		3.50	UV	0.2 M NaOH	0.1% Pt	52/ H_2	163
$PbTiO_3$		2.95	UV	10% methanol	1.0% Pt	70/ H_2	164
$BiFeO_3$ nanowires		2.35	> 380 nm	4 mM $FeCl_3$	1.0% Au	400/ H_2	165
$LaFeO_3$ nanoparticles		2.10	> 400 nm	10% methanol	W/O	8,600/ H_2	166
$LaTiO_2N$	O-site	2.10	> 420 nm	50 mM $AgNO_3$	2% CoO_x	3,680/ H_2	174
$(CaLa)TiO_{2.25}O_{0.75}$	O-site	2.00	> 420 nm	10 mM $AgNO_3$	2.0% IrO_2	500/O_2	175
$CaTaO_2N$	O-site	2.50	> 420 nm	20% methanol	0.3% Pt	250/ H_2	176
$BaTaO_2N$	O-site	2.00	> 420 nm	10 mM $AgNO_3$	1.5% IrO_2	500/ H_2	177
W-doped $BaTaO_2N$	B- and O-site	N/A	> 420 nm	10 mM $AgNO_3$	1.5% IrO_2	220/O_2	178
$SrTaO_2N$	O-site	2.10	> 420 nm	20% methanol	0.3% Pt	420/ H_2	179
$CaNbO_2N$	O-site	2.00	> 420 nm	10% methanol	1% Pt	10/ H_2	180
$(BaZrO_3)_x$–$(BaTaO_2N)_{1-x}$	O-site	N/A	> 420 nm	1 mM NaI	0.3% Pt	110/ H_2	181
$(BaZrO_3)_{0.05}$–$(BaTaO_2N)_{0.95}$	O-site	1.80	> 420 nm	1 mM NaI	0.3% Pt	440/ H_2	182
Double perovskites							
$LaMg_xTa_{1-x}O_{1+3x}N_{2-3x}$	O-site	1.9 to 2.1	> 420 nm	W/O	$RhCrO_y$	5/ H_2	183
$CaZrO_3$–$CaTaO_2N$	O-site	2.63	> 420 nm	10%	1.0% Pt	52.4/ H_2	184

nanoparticles				HCOOH			
$(SrTiO_3)_{1-x}(LaTiO_2N)_x$	O-site	2.00	> 420 nm	18% methanol	W/O	66.7/ H_2	185
$LaNi_{1-x}Cu_xO_3$ nanoparticles		2.5 to 2.8	> 400 nm	12.5% HCHO	W/O	1,180/ H_2	186
$Ba_2Bi_{1.4}Nb_{0.6}O_6$		1.64		1.0 M KOH	CoO_x	0.4 mA cm^{-2} @ 1.23 V_{RHE}	21
$Ba_2Bi(Bi_x, Nb_{1-x})O_6$ $(0 \le x \le 0.93)$		1.41~1.89	AM 1.5G	Neutral phosphate buffer	Pt	1 ~ 0.05 mA cm^{-2} @ 0 V_{RHE}	23
$NaTa_{1-x}Cu_xO_3$	A- and B-sites	2.8 to 3.4	> 415 nm	20% methanol	0.2% NiO	1,335/ H_2	187
$Ba_2Bi_{1.4}Nb_{0.6}O_6/WO_3$ nanosheets				1.0 M KOH	$CoMnO_x$	2.23 mA cm^{-2} @ 1.23 V_{RHE}	20
Beyond							
$La_2Ta_2ZrS_2O_8$	O-site	2.40	> 410 nm	10 mM $AgNO_3$	0.5% IrO_2	24/O_2	188
$La_2Ta_2ZrS_2O_8$	O-site		AM 1.5G	1.0 M NaOH	Co-Pi	0.02 mA cm^{-2} @ 1.23 V_{RHE}	188

However, single oxide perovskite usually has bandgaps (> 3.0 eV) too large for optimal photocatalytic applications. Elemental doping or alloying has been used to narrow their bandgaps. A number of dopants such as Cr, Mn, Ti, Ru, Rh, Ir, Er, and Zn have been used to reduce the bandgap of STO from 3.2 eV to as low as 1.9 eV (Ru-doping).[158-162] However, no significant improvements on photocatalytic performance were found, in particular for Mn-, Cu- doping.[159, 162] Wang *et al.* and Li *et al.* showed that Ta and Bi doping can reduce the bandgap to 1.70 and 2.64 eV, respectively, but their observed catalytic activities are inferior to that of $NaTaO_3$.[172, 173] Apart from cation doping, anion doping has also been used to reduce the band gap. N is the most common anion dopant for oxides. In some cases, the doping concentration can be high enough to form oxynitrides denoted as $AB(O,N)_3$.[174-185, 189, 190] Because the energy level of N 2*p* orbital is higher than that of O 2*p* orbital, bandgap of oxides can be reduced with N doping. For instance, $BaTaO_2N$ and $SrNbO_2N$ can harvest much wider range of visible light up to ca. 660 and 680 nm, respectively, which lead to theoretical solar-to-hydrogen (STH) conversion efficiencies of over 15%.[189] A particulate $BaTaO_2N$ photoanode prepared using a particle transfer method generated a photocurrent of 4.2 mA cm^{-2} at 1.2 V_{RHE}.[190] For N-doped titanates, $LaTiO_2N$ (LTON) is an *n*-type semiconductor with a bandgap of 2.1 eV (~600 nm absorption edge). IrO_2 loaded LTON was reported to achieve a quantum efficiency of ~5%, while CoO_x coated porous LTNO was able to reach a quantum efficiency of 27.1% at 440 nm, and it produced O_2 at a rate of 3,680 $\mu mol^{-1}g^{-1}h^{-1}$ in the presence of 50 mM $AgNO_3$.[174] Further Ca doping of LTNO to form $CaLaTiO_{2.25}N_{0.75}$ reduced the bandgap to 2.0 eV, but decreased the O_2 production rate to 500 $\mu mol^{-1}g^{-1}h^{-1}$, loaded with 2.0 wt% IrO_2 in presence of 10 mM $AgNO_3$.[175] Perovskite $LaMg_xTa_{1-x}O_{1+3x}N_{2-3x}$ (x >1/3) was reported to directly split water with visible light absorption up to 600 nm. Its quantum efficiency of overall water splitting reached ca. 0.03 % at 440 ± 30 nm.[183] S-doping is also a widely used

strategy for reducing the bandgap of oxides. For instance, perovskite oxysulfides, $La_2Ta_2ZrS_2O_8$, $La_2Ta_2TiS_2O_8$, and $La_2Nb_2TiS_2O_8$, are direct-bandgap semiconductors with absorption-edge wavelength up to 540, 700 and 700 nm, respectively.[188] The *d* orbitals of Zr, Ti contribute to the CBM, while the S 3*p* orbitals contribute to the VBM. A $La_2Ta_2ZrS_2O_8$ photoanode coated with CoPi electrocatalysts reached a photocurrent density of 300 μA cm^{-2} at 1.23 V V_{RHE} in a pH 13 electrolyte.[188]

Although the bandgap of single perovskite oxides can be reduced by oxynitrides and oxysulfides, the cation valence states can be difficult to maintain. For example, Nb/Ta cations in $BaNbO_2N$/$BaTaO_2N$ tend to be reduced during nitridation of metal oxides, resulting in low photocurrent density. Therefore, part of penta-valent Ta^{5+} in $BaTaO_2N$ were replaced by tetra or hexahydric-valent cations (Ti^{4+}, Zr^{4+}, Mo^{6+}, and W^{6+}) to control the donor density and the fabricated porous photoanodes achieved improved PEC performance under visible light.[191]

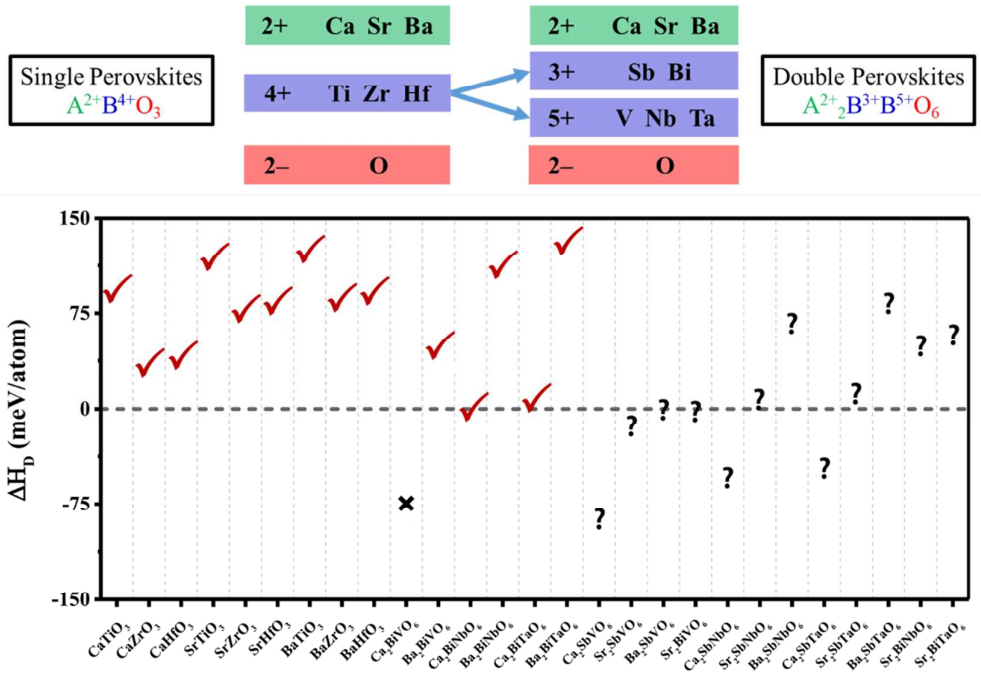

Fig. 8 The comparison of theory and experiments of the class of oxide double perovskites $A_2M(III)M(V)O_6$ (A= Ca, Sr, Ba; M(III) = Sb^{3+} or Bi^{3+}; M(V) = V^{5+}, Nb^{5+}, Ta^{5+}) and their parent ternary oxide perovskites $AM(IV)O_3$ (A= Ca, Sr, Ba; M(IV) = Ti^{4+}, Zr^{4+}, Hf^{4+}). Y-axis is the calculated decomposition energies of R-3 phase. '✓' means the compounds synthesized by experiments and perovskite phases can be found. '✗' means the compounds synthesized by experiments and perovskite phases cannot be found. '?' means the compounds without experimental report. Lower figure was reprinted with permission from Ref [19]. Copyright 2017, Wiley-VCH Verlag GmbH & Co. KGaA, Weinheim.

3.2.2 Double Perovskites by Chemical Mutation

Though doping or alloying can effectively narrow the bandgap of semiconductors, the incorporation of extrinsic dopants may introduce high density of defects that are harmful to device performance. In contrast, chemical mutation is known as one promising approach that can produce the derivatives with smaller bandgaps and without introducing detrimental defects.[192, 193] For example, the narrow bandgap (1.53 eV) semiconductor $CuInS_2$ can be deduced from ZnS with a bandgap of 3.78 eV through chemical mutation of Zn^{2+} → Cu^{1+} + In^{3+}. The strong coupling between Cu $3d^{10}$ and S $2p^6$ pushes up the VBM of $CuInS_2$ in energy position and therefore

narrows its bandgap. This strong *p-d* coupling additionally endows $CuInS_2$ with better defect tolerance. This method has been employed to design new oxide perovskites with narrow bandgaps and high defect tolerance desirable for PC applications.

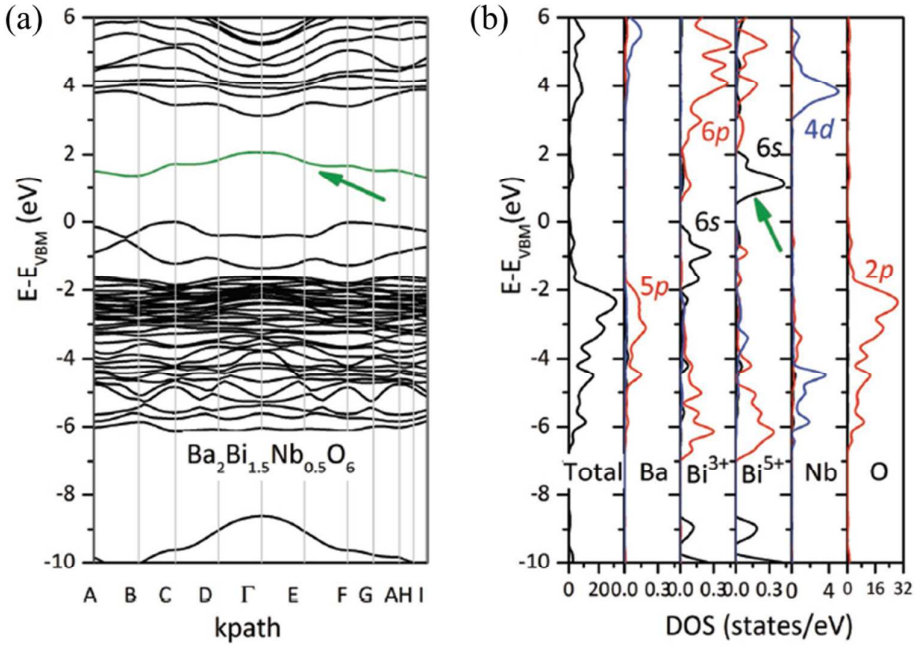

Fig. 9 a) Band structures and b) total and partial DOS of $Ba_2Bi_{1.5}Nb_{0.5}O_6$. Reprinted with permission from Ref [21]. Copyright 2017, Wiley-VCH Verlag GmbH & Co. KGaA, Weinheim.

With the mutation of Ti(IV) → M(III) + M(V), the prototype single perovskite $CaTiO_3$ can evolve into 18 double perovskites, $A_2M(III)M(V)O_6$ (see Fig. 11), where M(III) = group VA elements (Sb^{3+}, Bi^{3+}) with lone-pair s orbitals (i.e. occupied *s* orbitals), M(V) = group VB elements (V^{5+}, Nb^{5+}, Ta^{5+}), and A = group IIA elements (Ca^{2+}, Sr^{2+}, Ba^{2+})[19]. In these perovskites, the hybridization of the antibonding interaction between group VA elements (Sb^{3+}, Bi^{3+}) lone-pair *s* orbital and O 2*p* orbital can push up the valence bands to high-energy positions, therefore facilitate the *p*-type doping with defect tolerance and improve the valence band mismatch for water splitting.[21, 23] However, all these stoichiometric double perovskites still exhibit very large bandgaps (~3 eV or above).[19, 21] It was recently reported that the bandgap can be further reduced if the composition of these double perovskite oxides are M(III)-rich. In this case, the additional M(III) atoms occupy the M(V) sites and become M^{5+}, which introduces a new conduction band at a lower energy position, effectively reducing the bandgap. As an example, when additional Bi atoms are incorporated in Ba_2BiNbO_6 (BBNO), it leads to a general composition of $Ba_2Bi(Bi_x, Nb_{1-x})O_6$ ($0 \leq x < 1$). The Bi atoms occupying Nb sites have Bi^{5+} oxidation states. The low energy-lying unoccupied Bi^{5+} 6*s* orbital introduces a new conduction band edge (indicated by the arrow on Fig. 12) below the conduction band edge of pure BBNO, resulting in a much reduced bandgap, varying from ~1.4 eV at $x = 1$ to ~1.9 eV at $x = 0.07$.[21, 23] Recently, Ge *et al.* showed that Bi-rich $Ba_2Bi(Bi_x, Nb_{1-x})O_6$ photoelectrodes with $x = 0.4$~0.07 can produce cathodic photocurrents up to 0.2 mA·cm^{-2} at 0 V_{RHE} with positive onsets at ~1.5 V_{RHE} enabling unbiased water reduction.[23] Additionally, hybrid PEC cells with three electrodes that are optically stacked but electrically parallel to each other delivered anodic photocurrent densities up to 6.02 mA cm^{-2} at

1.23 V_{RHE}.[20]

3.3 Photovoltaics

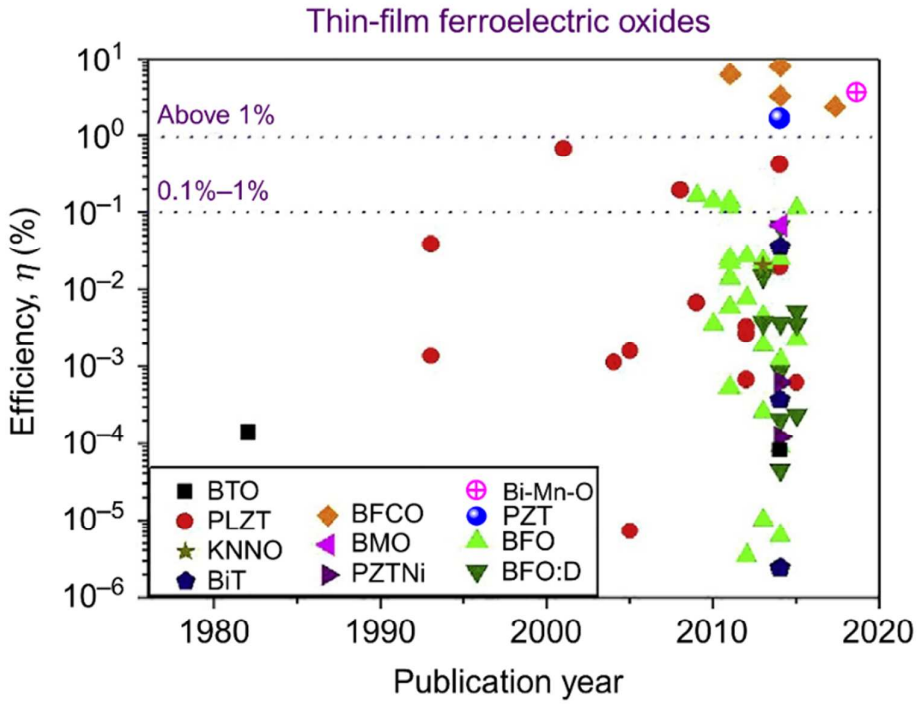

Fig. 10 A timeline plot for the reported PV device efficiencies of thin-film single layer ferroelectric oxides. BTO ($BaTiO_3$), $Pb(Zr,Ti)O_3$ (PZT), PLZT ($(Pb,La)(Zr,Ti)O_3$), KNNO ($K_xNa_{1-x}NbO_3$) and BiT (layered ferroelectrics $Bi_4Ti_3O_{12}$, $Bi_5FeTi_3O_{15}$, or $Bi_x(Na,K)_{1-x}Ti_3O_{15}$) are wide bandgap ferroelectric oxide semiconductors with an optical bandgap in the near ultraviolet range, i.e., 3-4 eV. BFCO (Bi_2FeCrO_6), BMO ($Bi_xMn_{1-x}O_3$), and PZTNi ($PZT+NiO_x$) are ferroelectric oxides with an optical bandgap in the range of 1-2 eV suitable for harvesting solar light with higher theoretical efficiencies. BFO ($BiFeO_3$) (and doped BFO, BFO:D) has an optical bandgap somewhere in between ranging 2.2-2.7 eV. Three materials with efficiencies above 1% are PZT ($Pb(Zr,Ti)O_3$) thin-film (~1.25%), Bi-Mn-O (mixed $BiMnO_3$ and $BiMn_2O_5$) thin-film (~4.20%) and BFCO (Bi_2FeCrO_6) based *p-i-n* heterojunction photovoltaic devices (~2%). Reprinted with permission from ref [24] with addition of Bi-Mn-O system [194], $Pb(Zr,Ti)O_3$ system [195] and a BFCO based p-i-n heterojunction PV device [196].

Oxide perovskites and related materials have also been used as absorbers for PV applications. Two types of solar cells have been explored. The first type uses the ferroelectric properties seen in ferroelectric oxide perovskites $BaTiO_3$[197, 198]. In this type of solar cells, the photo-excited carriers are separated by the polarization-induced internal electric field,[199] rather than the electric field developed at the *p-n* junctions in conventional solar cells. Such solar cells can generate open-circuit voltage (V_{oc}) exceeding the bandgap of the absorber material.[200-202] Dharmadhikari *et al.* reported the thin-film ferroelectric PV device based on $BaTiO_3$ in 1982,[203] then followed by the reports on $LiNbO_3$-, $(Pb,La)TiO_3$-, $Pb(Zr,Ti)O_3$ (PZT)- and $(Pb,La)(Zr,Ti)O_3$-based solar cells (Fig. 14). However, these PV devices showed low power conversion efficiencies (PCEs), due to very low short-circuit current density (J_{sc}) typically in the range of nA- μA cm^{-2}.[24] The low J_{sc}

cannot be fully explained by the large bandgaps of the absorbers. For example, multiferroic $BiFeO_3$ (BFO) has a relatively small bandgap of ~2.7 eV that just straddles into visible light region[204]. BFO-based all-oxide PV devices can exhibit enhanced J_{SC}'s within the range of 1-1.5 mA cm^{-2} when illuminated by a 150 W Xenon lamp with a 2.85 suns light intensity.[205] However, under a standard AM 1.5 G illumination, the BFO PV devices only produced very small J_{SC}'s roughly on the order of μA cm^{-2}.[24]

Another type of solar cells using oxide perovskites and related materials as absorbers that involve other effects in additional to ferroelectric properties. Recently, a ~4.2% efficiency PV cell has been achieved under one sun illumination, using a mixed absorber consisting of a small bandgap ferroelectric $BiMnO_3$ (1.2 eV) and non-ferroelectric $BiMn_2O_5$ semiconductor (1.23 eV).[194] This oxide perovskite-based solar cell showed a much higher J_{sc} of ~7.03 mA cm^{-2}. Double perovskite Bi_2FeCrO_6 (BFCO), which can be considered as a solid solution of $BiFeO_3$ and $BiCrO_3$, demonstrated tunable bandgaps from 2.1 eV to 1.4 eV by varying the Fe/Cr cation ordering. The low-bandgap BFCO absorber led to greatly increased J_{SC} of 11.7 mA cm^{-2} in a single layer solar cell. The multilayer heterostructure-based solar cells exhibited even higher PCEs (up to 8.1%) under standard AM 1.5G illumination.[70] Oxide perovskites containing 3*d* transition metals (TMs) typically have large carrier effective masses due to the nondispersive band edges derived from the localized 3*d* orbitals (Table 8), which lead to low carrier mobilities and high carrier recombination, limiting the PCEs. As shown above, the non-3*d* TM-containing oxide double perovskites, $A_2M(III)M(V)O_6$, can exhibit both lower bandgaps and smaller carrier effective masses, which can be attractive absorbers for PV applications.

Tab. 8. The comparison of calculated electron and hole effective masses for $A_2M(III)M(V)O_6$ double perovksites and typical ferroelectric perovskites.

	Electron effective mass (m_0)	**Hole effective mass (m_0)**
$A_2M(III)M(V)O_6$ double perovksites[19]		
Ba_2BiVO_6	0.87	0.27
Ba_2BiNbO_6	0.52	0.39
Ba_2BiTaO_6	0.51	0.39
Ba_2SbNbO_6	0.48	0.30
Ba_2SbTaO_6	0.48	0.33
Ferroelectric Perovskite[206]		
$KNbO_3$	1.56	2.74
$BaTiO_3$	0.48	1.08
$BiFeO_3$	0.69	3.17

4. Conclusion and Perspective

We have reviewed structural and compositional flexibility, the chemical and thermal stabilities of oxide perovskites and their derivatives, and their versatile applications in EC, PC, and PV. Though significant progress has been made, more are anticipated since there are still a large number of oxide perovskites and derivatives that are theoretically predicted to exist, but have not been explored experimentally.

For EC applications, the current research is mainly driven by the activity descriptors. Identification of a more appropriate descriptor may facilitate new materials design. Descriptors

that establish reliable relationships between the constituent elements and the desired properties and also provide clear guidance for the experimental synthesis are highly desirable. Such descriptors will help screen the large number of oxide perovskites and derivatives with better properties for EC applications.

For PC and PV applications, the absorber materials require strong sunlight absorption, small carrier effective masses and high defect tolerance. The recently proposed non-3*d* TM-containing oxide double perovskites, $A_2M(III)M(V)O_6$, can potentially meet these requirements. As seen in Fig. 11, many of the predicted $A_2M(III)M(V)O_6$, have not been experimentally reported. These newly theoretically designed oxides may lead to PC and PV devices with much enhanced performance.

Because of the extreme structural and compositional flexibility, there are unlimited numbers of oxide perovskites and related materials that may exhibit versatile electrical and optoelectronic properties. Identify appropriate applications in EC, PC, and PV of all these oxides can be extremely challenging. High-throughput calculations and machine learning can unravel the hidden relationship between structure, composition, and physical properties of materials.[207-211] We anticipate that machine learning may help expedite the discovery of promising candidates of oxide perovskites and relative materials for efficient EC, PC, and PV devices.

Conflicts of interest

There are no conflicts to declare.

Acknowledgements

W.-J.Y. acknowledges the funding support from National Key R&D Program of China under Grant No. 2016YFB0700700, National Natural Science Foundation of China (under Grant No. 51602211, No. 11674237), Natural Science Foundation of Jiangsu Province of China (under Grant No. BK20160299), National Young Talent 1000 Program and Jiangsu Double-Talent Program. B. W and Y. Y. acknowledge financial support by US NSF project No. CBET-1433401 competitively selected under the solicitation "NSF 14-15: NSF/DOE Partnership on Advanced Frontiers in Renewable Hydrogen Fuel Production via Solar Water Splitting Technologies", which was co-sponsored by the National Science Foundation, Division of Chemical, Bioengineering, Environmental, and Transport Systems (CBET), and the U.S. Department of Energy, Office of Energy Efficiency and Renewable Energy, Fuel Cell Technologies Office. J. G. acknowledges Brain Korea 21 Program for Leading Universities & Students (BK 21 PLUS, No. 21A20131912052) of Seoul National University.

References

1. M. G. Walter, E. L. Warren, J. R. McKone, S. W. Boettcher, Q. Mi, E. A. Santori and N. S. Lewis, *Chem. Rev.*, 2010, **110**, 6446-6473.
2. S. W. Boettcher, E. L. Warren, M. C. Putnam, E. A. Santori, D. Turner-Evans, M. D. Kelzenberg, M. G. Walter, J. R. McKone, B. S. Brunschwig, H. A. Atwater and N. S. Lewis, *J. Am. Chem. Soc.*, 2011, **133**, 1216-1219.
3. S. W. Boettcher, J. M. Spurgeon, M. C. Putnam, E. L. Warren, D. B. Turner-Evans, M. D. Kelzenberg, J. R. Maiolo, H. A. Atwater and N. S. Lewis, *Science*, 2010, **327**, 185-187.
4. Y. W. Chen, J. D. Prange, S. Dühnen, Y. Park, M. Gunji, C. E. Chidsey and P. C. McIntyre, *Nat. Mater.*, 2011, **10**, 539-544.
5. A. Fujishima and K. Honda, *Nature*, 1972, **238**, 37-38.
6. A. Kudo and Y. Miseki, *Chem. Soc. Rev.*, 2009, **38**, 253-278.
7. M. D. Hernández-Alonso, F. Fresno, S. Suárez and J. M. Coronado, *Energy Environ. Sci.*, 2009, **2**, 1231-1257.
8. J. Zhang, Z. Zhao, Z. Xia and L. Dai, *Nat. Nanotechnol.*, 2015, **10**, 444-452.
9. P. G. Bruce, S. A. Freunberger, L. J. Hardwick and J.M. Tarascon, *Nat. Mater.*, 2012, **11**, 19-29.
10. H. A. Gasteiger and N. M. Markovic, *Science*, 2009, **324**, 48-49.
11. M. Armand and J. M. Tarascon, *Nature*, 2008, **451**, 652-657.
12. T. R. Cook, D. K. Dogutan, S. Y. Reece, Y. Surendranath, T. S. Teets and D. G. Nocera, *Chem. Rev.*, 2010, **110**, 6474-6502.
13. M. A. Green and S. P. Bremner, *Nat. Mater.*, 2017, **16**, 23-34.
14. S. Zhu, and D. Wang, *Adv. Energy Mater.,* 2017, **7**, 1700841.
15. Y. Goto, T. Hisatomi, Q. Wang, T. Higashi, K. Ishikiriyama, T. Maeda, Y. Sakata, S. Okunaka, H. Tokudome, M. Katayama, S. Akiyama, H. Nishiyama, Y. Inoue, T. Takewaki, T. Setoyama, T. Minegishi, T. Takata, T. Yamada, and K. Domen, *Joule*, 2018, **2**, 509-520.
16. Y. H. Huang, R. I. Dass, Z. L. Xing and J. B. Goodenough, *Science*, 2006, **312**, 254-257.
17. B. Weng, F. Xu, C. Wang, W. Meng, C. R. Grice and Y. Yan, *Energy Environ. Sci.*, 2017, **10**, 121-128.
18. O. S. Bushuyev, P.D. Luna, C. T. Dinh, L. Tao, G. Saur, J. van de Lagemaat, S. O. Kelley, E. H. Sargent, *Joule*, 2018, **2**, 825-832.
19. Q. Sun, J. Wang, W.-J. Yin and Y. Yan, *Adv. Mater.*, 2018, **30**, 1705901.
20. B. Weng, C. R. Grice, J. Ge, T. Poudel, X. Deng and Y. Yan, *Adv. Energy Mater.*, 2018, **8**, 1701655.
21. B. Weng, Z. Xiao, W. Meng, C. R. Grice, T. Poudel, X. Deng and Y. Yan, *Adv. Energy Mater.*, 2017, **7**, 1602260.
22. Grinberg, D. V. West, M. Torres, G. Gou, D. M. Stein, L. Wu, G. Chen, E. M. Gallo, A. R. Akbashev, P. K. Davies, J. E. Spanier and A. M. Rappe, *Nature*, 2013, **503**, 509-512.
23. J. Ge, W.-J. Yin and Y. Yan, *Chem. Mater.*, 2018, **30**, 1017-1031.

24. A. Pérez-Tomás, A. Mingorance, D. Tanenbaum and M. Lira-Cantú, Metal Oxides in Photovoltaics:All-Oxide, Ferroic, and Perovskite Solar Cells In The Future of Semiconductor Oxides in Next-Generation Solar Cells, Barcelona, Spain, 2018.
25. M. A. Pena and J. L. G. Fierro, *Chem. Rev.*, 2001, **101**, 1981-2018.
26. R. E. Cohen, *Nature*, 1992, **358**, 136-138.
27. A. Kojima, K. Teshima, Y. Shirai and T. Miyasaka, *J. Am. Chem. Soc.*, 2009, **131**, 6050-6051.
28. H.-S. Kim, C.-R. Lee, J.-H. Im, K.-B. Lee, T. Moehl, A. Marchioro, S.-J. Moon, R. Humphry-Baker, J.-H. Yum, J. E. Moser, M. Graetzel and N.-G. Park, *Sci. Rep.*, 2012, **2**, 591.
29. J. Burschka, N. Pellet, S.-J. Moon, R. Humphry-Baker, P. Gao, M. K. Nazeeruddin and M. Grätzel, Nature, 2013, **499**, 316-319.
30. M. M. Lee, J. Teuscher, T. Miyasaka, T. N. Murakami and H. J. Snaith, *Science*, 2012, **338**, 643-647.
31. M. T. Anderson, K. B. Greenwood, G. A. Taylor and K. R. Poeppelmeier, Prog. *Solid State Chem.*, 1993, **22**, 197-233.
32. S. Vasala and M. Karppinen, *Prog. Solid State Chem.*, 2015, **43**, 1-36.
33. M. W. Lufaso, P. W. Barnes and P. M. Woodward, *Acta Crystallogr., Sect. B: Struct. Sci.*, 2006, **62**, 397-410.
34. F. Shojaei and W.-J. Yin, J. Phys. Chem. C, 2018, **122**, 15214-15219.
35. A. M. Glazer, *Acta Crystallogr., Sect. B: Struct. Sci.*, 1972, **B 28**, 3384-3392.
36. C. J. Howard and H. T. Stokes, *Acta Crystallogr., Sect. B: Struct. Sci.*, 1998, **54**, 782-789.
37. M. W. Lufaso and P. M. Woodward, *Acta Crystallogr., Sect. B: Struct. Sci.*, 2001, **57**, 725-738.
38. W. J. Yin, T. T. Shi and Y. Yan, *Adv. Mater.*, 2014, **26**, 4653-4658.
39. H. Lin, C. Zhou, Y. Tian, T. Siegrist and B. Ma, *ACS Energy Lett.*, 2018, **3**, 54-62.
40. F. Song and X. Hu, *J. Am. Chem. Soc.*, 2014, **136**, 16481-16484.
41. W. Pies and A. Weiss, in Crystal Structure Data of Inorganic Compounds, Numerical Data and Functional Relationships in Science and Technology Group III: Crystal and Solid State Physics, eds. K.-H. Hellwege and A. M. Hellwege, Springer-Verlag, Berlin-Heidelberg-NewYork 1976, vol. 7 Part e, ch. Crystal Structure Data of Inorganic Compounds.
42. J. Suntivich, K. J. May, H. A. Gasteiger, J. B. Goodenough and Y. Shao-Horn, *Science*, 2011, **334**, 1383-1385.
43. X. Cheng, E. Fabbri, M. Nachtegaal, I. E. Castelli, M. El Kazzi, R. Haumont, N. Marzari and T. J. Schmidt, *Chem. Mater.*, 2015, **27**, 7662-7672.
44. H. W. Park, D. U. Lee, P. Zamani, M. H. Seo, L. F. Zazar and Z. Chen, *Nano Energy*, 2014, **10**, 192-200.
45. J.-I. Jung, H. Y. Jeong, J.-S. Lee, M. G. Kim and J. Cho, *Angew. Chem., Int. Ed.*, 2014, **53**, 4582-4586.
46. Y. Zhu, W. Zhou, Z.-G. Chen, Y. Chen, C. Su, M. O. Tade and Z. Shao, *Angew. Chem., Int. Ed.*, 2015, **54**, 3897-3901.
47. W. Zhou, M. Zhao, F. Liang, S. C. Smith and Z. Zhu, *Mater. Horiz.*, 2015, **2**, 495-501.
48. J.-I. Jung, M. Risch, S. Park, M. G. Kim, G. Nam, H.-Y. Jeong, Y. Shao-Horn and J. Cho, *Energy Environ. Sci.*, 2016, **9**, 176-183.
49. A. Grimaud, K. J. May, C. E. Carlton, Y.-L. Lee, M. Risch, W. T. Hong, J. Zhou and Y. Shao-Horn, *Nat. Commun.*, 2013, **4**, 2439.

50. K. Elumeeva, J. Masa, F. Tietz, F. Yang, W. Xia, M. Muhler and W. Schuhmann, *ChemElectroChem*, 2016, **3**, 138-143.
51. J. M. Christ, C. Ngo, T. Batson, C. A. Cadigan, J. Tong, R. M. Richards, R. O'Hayre and S. Pylypenko, *Catal. Sci. Technol.*, 2016, **6**, 7744-7751.
52. R. S. Kalubarme, G.-E. Park, K.-N. Jung, K.-H. Shin, W.-H. Ryu and C.-J. Park, *J. Electrochem. Soc*., 2014, **161**, A880-A889.
53. Z. Wang, Y. You, J. Yuan, Y.-X. Yin, Y.-T. Li, S. Xin and D. Zhang, *ACS Appl. Mater. Interfaces*, 2016, **8**, 6520-6528.
54. X. Zhang, Y. Gong, S. Li and C. Sun, *ACS Catal.*, 2017, **7**, 7737-7747.
55. Y. Guo, Y. Tong, P. Chen, K. Xu, J. Zhao, Y. Lin, W. Chu, Z. Peng, C. Wu and Y. Xie, Adv. Mater., 2015, **27**, 5989-5994.
56. K. J. May, C. E. Carlton, K. A. Stoerzinger, M. Risch, J. Suntivich, Y.-L. Lee, A. Grimaud and Y. Shao-Horn, *J. Phys. Chem. Lett.*, 2012, **3**, 3264-3270.
57. D.-G. Lee, O. Gwon, H.-S. Park, S. H. Kim, J. Yang, S. K. Kwak, G. Kim and H.-K. Song, *Angew. Chem., Int. Ed.*, 2015, **54**, 15730-15733.
58. J. Kim, X. Yin, K.-C. Tsao, S. Fang and H. Yang, *J. Am. Chem. Soc.*, 2014, **136**, 14646-14649.
59. C. Jin, Z. Yang, X. Cao, F. Lu and R. Yang, *Int. J. Hydrogen Energy*, 2014, **39**, 2526-2530.
60. F. Lu, J. Sui, J. Su, C. Jin, M. Shen and R. Yang, *J. Power Sources*, 2014, **271**, 55-59.
61. D. Zhang, Y. Song, Z. Du, L. Wang, Y. Li and J. B. Goodenough, *J. Mater. Chem. A*, 2015, **3**, 9421-9426.
62. Z. Wu, L.-P. Sun, T. Xia, L.-H. Huo, H. Zhao, A. Rougier and J.-C. Grenier, *J. Power Sources*, 2016, **334**, 86-93.
63. X. Ge, F. W. T. Goh, B. Li, T. S. A. Hor, J. Zhang, P. Xiao, X. Wang, Y. Zong and Z. Liu, *Nanoscale*, 2015, **7**, 9046-9054.
64. W. T. Hong, R. E. Welsch and Y. Shao-Horn, *J. Phys. Chem. C*, 2016, **120**, 78-86.
65. F. Zheng, Y. Xin, W. Huang, J. Zhang, X. Wang, M. Shen, W. Dong, L. Fang, Y. Bai, X. Shen and J. Hao, *J. Mater. Chem. A*, 2014, **2**, 1363-1368.
66. C. Su, W. Wang, Y. Chen, G. Yang, X. Xu, M. O. Tade and Z. Shao, *ACS Appl. Mater. Interfaces*, 2015, **7**, 17663-17670.
67. B. Zhao, L. Zhang, D. Zhen, S. Yoo, Y. Ding, D. Chen, Y. Chen, Q. Zhang, B. Doyle, X. Xiong and M. Liu, *Nat. Commun.*, 2017, **8**, 14586.
68. Z. Du, P. Yang, L. Wang, Y. Lu, J. B. Goodenough, J. Zhang and D. Zhang, *J. Power Sources*, 2014, **265**, 91-96.
69. M. Prabu, P. Ramakrishnan, P. Ganesan, A. Manthiram and S. Shanmugam, *Nano Energy*, 2015, **15**, 92-103.
70. R. Nechache, C. Harnagea, S. Li, L. Cardenas, W. Huang, J. Chakrabartty and F. Rosei, *Nat. Photonics*, 2015, **9**, 61-67.
71. S. Li, B. AlOtaibi, W. Huang, Z. Mi, N. Serpone, R. Nechache and F. Rosei, *Small*, 2015, **11**, 4018-4026.
72. S. Yagi, I. Yamada, H. Tsukasaki, A. Seno, M. Murakami, H. Fujii, H. Chen, N. Umezawa, H. Abe, N. Nishiyama and S. Mori, *Nat. Commun.,* 2015, **6**, 8249.
73. J. H. Clark, M. S. Dyer, R. G. Palgrave, C. P. Ireland, J. R. Darwent, J. B. Claridge and M. J. Rosseinsky, *J. Am. Chem. Soc.,* 2011, **133**, 1016-1032.
74. H. Sun, G. Chen, Y. Zhu, B. Liu, W. Zhou and Z. Shao, *Chem-Euro. J.,* 2017, **23**, 5722-5728.

75. M. Gong, Y. Li, H. Wang, Y. Liang, J. Z. Wu, J. Zhou, J. Wang, T. Regier, F. Wei and H. Dai, *J. Am. Chem. Soc.,* 2013, **135**, 8452-8455.
76. X. Long, J. Li, S. Xiao, K. Yan, Z. Wang, H. Chen and S. Yang, *Angew. Chem. Int. Ed.,* 2014, **126**, 7714-7718.
77. R. J. D. Tilley, *Perovskites-Structure-Property Relationship*, Wiley, 2016.
78. W.-J. Li and Z.-W. Fu, *Appl. Surf. Sci.,* 2010, **256**, 2447-2452.
79. A. A. Colville and S. Geller, *Acta Crystallographica Section B-Structural Crystallography and Crystal Chemistry*, 1971, **B 27**, 2311-2315.
80. G. Rothenberg, *Catalysis: Concepts and Green Applications*, Wiley-VCH., 2008.
81. J. Hwang, R. R. Rao, L. Giordano, Y. Katayama, Y. Yu and Y. Shao-Horn, *Science*, 2017, **358**, 751-756.
82. W. G. Hardin, D. A. Slanac, X. Wang, S. Dai, K. P. Johnston and K. J. Stevenson, *J. Phys. Chem. Lett.,* 2013, **4**, 1254-1259.
83. W. G. Hardin, J. T. Mefford, D. A. Slanac, B. B. Patel, X. Wang, S. Dai, X. Zhao, R. S. Ruoff, K. P. Johnston and K. J. Stevenson, *Chem. Mater.,* 2014, **26**, 3368-3376.
84. Y. Matsumoto and E. Sato, *Mater. Chem. Phys.,* 1986, **14**, 397-426.
85. Y. Matsumoto, J. Kurimoto and E. Sato, *J. Electroanal. Chem.,* 1979, **102**, 77-83.
86. X. Han, T. Zhang, J. Du, F. Cheng and J. Chen, *Chem. Sci.,* 2013, **4**, 368-376.
87. B. R. Wygant, K. A. Jarvis, W. D. Chemelewski, O. Mabayoje, H. Celio and C. B. Mullins, *ACS Catal*., 2016, **6**, 1122-1133.
88. Y. Zhao, L. Xu, L. Mai, C. Han, Q. An, X. Xu, X. Liu and Q. Zhang, *P. Natl. Acad. Sci. USA.,* 2012, **109**, 19569-19574.
89. M. Y. Oh, J. S. Jeon, J. J. Lee, P. Kim and K. S. Nahm, *Rsc Adv.*, 2015, **5**, 19190-19198.
90. H. W. Park, D. U. Lee, M. G. Park, R. Ahmed, M. H. Seo, L. F. Nazar and Z. Chen, *ChemSusChem*, 2015, **8**, 1058-1065.
91. R. A. Rincon, J. Masa, S. Mehrpour, F. Tietz and W. Schuhmann, *Chem. Commun.,* 2014, **50**, 14760-14762.
92. J.-I. Jung, H. Y. Jeong, M. G. Kim, G. Nam, J. Park and J. Cho, *Adv. Mater*., 2015, **27**, 266-271.
93. Y. Zhu, W. Zhou, Y. Zhong, Y. Bu, X. Chen, Q. Zhong, M. Liu and Z. Shao, *Adv. Energy Mater.,* 2017, **7**, 1602122.
94. H. Sun, G. Chen, J. Sunarso, J. Dai, W. Zhou and Z. Shao, *ACS Appl. Mater. Inter.,* 2018, 10, 16939-16942.
95. G. Chen, Z. Hu, Y. Zhu, Z. G. Chen, Y. Zhong, H. J. Lin, C. T. Chen, H. Tjeng, W. Zhou, Z. Shao, *J. Mater. Chem. A*, 2018, 6, 9854-9859.
96. Z. Li, L. Lv, J. Wang, X. Ao, Y. Ruan, D. Zha, G. Hong, Q. Wu, Y. Lan, C. Wang, J. Jiang and M. Liu, *Nano Energy*, 2018, **47**, 199-209.
97. Suntivich, H. A. Gasteiger, N. Yabuuchi and Y. Shao-Horn, *J. Electrochem. Soc*., 2010, **157**, B1263-B1268.
98. B. Hua, Y.-F. Sun, M. Li, N. Yan, J. Chen, Y.-Q. Zhang, Y. Zeng, B. S. Amirkhiz and J.-L. Luo, *Chem. Mater.,* 2017, **29**, 6228-6237.
99. Y. Zhan, C. Xu, M. Lu, Z. Liu and J. Y. Lee, *J. Mater. Chem. A,* 2014, **2**, 16217-16223.
100. Y. Zhu, W. Zhou, J. Yu, Y. Chen, M. Liu and Z. Shao, *Chem. Mater.,* 2016, **28**, 1691-1697.
101. Y. Zhu, W. Zhou, J. Sunarso, Y. Zhong and Z. Shao, *Adv. Funct. Mater.,* 2016, **26**, 5862-5872.

102. H. Liu, X. Ding, L. Wang, D. Ding, S. Zhang and G. Yuan, *Electrochimica. Acta.,* 2018, **259**, 1004-1010.
103. S. Liu, H. Luo, Y. Li, Q. Liu and J.-L. Luo, *Nano Energy*, 2017, **40**, 115-121.
104. Y. Bu, O. Gwon, G. Nam, H. Jang, S. Kim, Q. Zhong, J. Cho and G. Kim, *ACS Nano,* 2017, **11**, 11594-11601.
105. J. Wang, Y. Gao, D. Chen, J. Liu, Z. Zhang, Z. Shao and F. Ciucci, *ACS Catal.,* 2018, **8**, 364-371.
106. F. Song, K. Schenk and X. Hu, *Energy Environ. Sci.,* 2016, **9**, 473-477.
107. D. Meadowcroft, *Nature*, 1970, **226**, 847-848.
108. Y. Matsumoto, H. Yoneyama and H. Tamura, *J. Electroanal. Chem.,* 1977, **79**, 319-326.
109. J. O. Bockris and T. Otagawa, *J. Electrochem. Soc.,* 1984, **131**, 290-302.
110. T. Hyodo, M. Hayashi, N. Miura and N. Yamazoe,*J. Electrochem. Soc.,* 1996, **143**, 266-267.
111. J. Sunarso, A. A. Torriero, W. Zhou, P. C. Howlett and M. Forsyth, *J. Phys. Chem. C*, 2012, **116**, 5827-5834.
112. C. Zhu, A. Nobuta, I. Nakatsugawa and T. Akiyama, *Int. J. Hydrogen Energy,* 2013, **38**, 13238-13248.
113. C. Man, H.-Y. Su, F. Calle-Vallejo, H. A. Hansen, J. I. Martinez, N. G. Inoglu, J. Kitchin, T. F. Jaramillo, J. K. Norskov and J. Rossmeisl, *Chemcatchem*, 2011, **3**, 1159-1165.
114. R. A. Rincón, E. Ventosa, F. Tietz, J. Masa, S. Seisel, V. Kuznetsov and W. Schuhmann, *Chem PhysChem,* 2014, **15**, 2810-2816.
115. M. Yuasa, N. Tachibana and K. Shimanoe, *Chem. Mater.,* 2013, **25**, 3072-3079.
116. H. Obayashi and T. Kudo, *Mater. Res. Bull.,* 1978, **13**, 1409-1413.
117. S. K. Tiwari, P. Chartier and R. N. Singh, *J. Electrochem. Soc*., 1995, **142**, 148-153.
118. H. Kozuka, K. Ohbayashi and K. Koumoto, *Sci. Technol. Adv. Mater*., 2015, **16**, 026001.
119. F. Azizi, A. Kahoul and A. Azizi, *J. Alloy. .Compd*., 2009, **484**, 555-560.
120. Z. P. Shao and S. M. Haile, *Nature*, 2004, **431**, 170-173.
121. P. Zeng, Z. Chen, W. Zhou, H. Gu, Z. Shao and S. Liu, *J. Membrane Sci*., 2007, **291**, 148-156.
122. D. Chen and Z. Shao, *Int. J. Hydrogen Energy,* 2011, **36**, 6948-6956.
123. Z. P. Shao, W. S. Yang, Y. Cong, H. Dong, J. H. Tong and G. X. Xiong, *J. Membrane Sci*., 2000, **172**, 177-188.
124. Y. Hori, A. Murata, R. Takahashi and S. Suzuki, *J. Am. Chem. Soc.,* 1987, **109**, 5022-5023.
125. A. Broussard and L. E. Wade, *Prep. Am. Chem. Soc. Pap. Div. Fuel Chem.*, 1986, **31**, 75.
126. R. Watson and G. A. Somorjai, *J. Catal.*, 1982, **74**, 282-295.
127. M. Schwartz, R. L. Cook, V. M. Kehoe, R. C. Macduff, J. Patel and A. F. Sammells, *J. Electrochem. Soc*., 1993, **140**, 614-618.
128. K.-N. Jung, J.-H. Jung, W. B. Im, S. Yoon, K.-H. Shin and J.-W. Lee, *ACS Appl. Mater. Interfaces,* 2013, **5**, 9902-9907.
129. A. Duprat, P. Alphonse, C. Sarda, A. Rousset and B. Gillot, *Mater. Chem. Phys*., 1994, **37**, 76-81.
130. X.-Z. Yuan, X. Li, W. Qu, D. G. Ivey and H. Wang, *ECS Trans.,* 2011, **35**, 11-20.
131. C. Seitz, C. F. Dickens, K. Nishio, Y. Hikita, J. Montoya, A. Doyle, C. Kirk, A. Vojvodic, H. Y. Hwang and J. K. Norskov, *Science*, 2016, **353**, 1011-1014.
132. L. Trotochaud, J. K. Ranney, K. N. Williams and S. W. Boettcher, *J. Am. Chem. Soc.,* 2012, **134**, 17253-17261.

133. M. Wehrens-Dijksma and P. H. L. Notten, *Electrochim. Acta,* 2006, **51**, 3609-3621.
134. X. Zou, A. Goswami and T. Asefa, *J. Am. Chem. Soc.,* 2013, **135**, 17242-17245.
135. J. Luo, J.-H. Im, M. T. Mayer, M. Schreier, M. K. Nazeeruddin, N.-G. Park, S. D. Tilley, H. J. Fan and M. Grätzel, *Science*, 2014, **345**, 1593-1596.
136. J. H. Montoya, L. C. Seitz, P. Chakthranont, A. Vojvodic, T. F. Jaramillo and J. K. Nørskov, *Nat. Mater.*, 2017, **16**, 70-81.
137. N. Armaroli and V. Balzani, *Angew. Chem. Int. Ed*., 2007, **46**, 52-66.
138. R. Asahi, T. Morikawa, T. Ohwaki, K. Aoki and Y. Taga, *Science*, 2001, **293**, 269-271.
139. X. Chen, S. Shen, L. Guo and S. S. Mao, *Chem. Rev.*, 2010, **110**, 6503-6570.
140. U. Khan, M. Al-Shahry and W. B. Ingler, *Science*, 2002, **297**, 2243-2245.
141. D. Kim, K. K. Sakimoto, D. Hong and P. Yang, *Angew. Chem. Int. Ed.*, 2015, **54**, 3259-3266.
142. B. Liu, C.-H. Wu, J. Miao and P. Yang, *ACS Nano*, 2014, **8**, 11739-11744.
143. K. Maeda, T. Takata, M. Hara, N. Saito, Y. Inoue, H. Kobayashi and K. Domen, *J. Am. Chem. Soc.*, 2005, **127**, 8286-8287.
144. Z. Zhang and J. T. Yates Jr, *Chem. Rev.*, 2012, **112**, 5520-5551.
145. L. Ji, M. D. McDaniel, S. Wang, A. B. Posadas, X. Li, H. Huang, J. C. Lee, A. A. Demkov, A. J. Bard and J. G. Ekerdt, *Nat. Nanotechnol.*, 2015, **10**, 84-90.
146. J. Liu, G. Chen, Z. Li and Z. Zhang, *Int. J. Hydrogen Energy*, 2007, **32**, 2269-2272.
147. H. Kato, K. Asakura and A. Kudo, *J. Am. Chem. Soc.*, 2003, **125**, 3082-3089.
148. H. Kato, H. Kobayashi and A. Kudo, *J. Phys. Chem. B*, 2002, **106**, 12441-12447.
149. H. Kato and A. Kudo, *J. Phys. Chem. B*, 2001, **105**, 4285-4292.
150. X. Xu, C. Randorn, P. Efstathiou and J. T. Irvine, *Nat. Mater.*, 2012, **11**, 595-598.
151. D. Arney, C. Hardy, B. Greve and P. A. Maggard, *J. Photochem. Photobiol. A*, 2010, **214**, 54-60.
152. Q.-P. Ding, Y.-P. Yuan, X. Xiong, R.-P. Li, H.-B. Huang, Z.-S. Li, T. Yu, Z.-G. Zou and S.-G. Yang, *J. Phys. Chem. C*, 2008, **112**, 18846-18848.
153. K. Townsend, N. D. Browning and F. E. Osterloh, *ACS Nano*, 2012, **6**, 7420-7426.
154. Shoji, G. Yin, M. Nishikawa, D. Atarashi, E. Sakai, and M. Miyauchi, *Chem. Phys. Lett*. 2016, **658**, 309-314.
155. Y. Bi, L. Zong, C. Li, Q. Li, and J. Yang, *Nanoscale Res. Lett*. 2015, **10**, 345.
156. H. Yoshida, L. Zhang, M. Sato, T. Morikawa, T. Kajino, T. Sekito, S. Matsumoto, and H. Hirata, *Catal. Today* 2015, **251**, 132-139.
157. H. Nakanishi, K. Iizuka, T. Takayama, A. Iwase, and A. Kudo, *ChemSusChem* 2017, **10**, 112-118.
158. H. Yu, S. Ouyang, S. Yan, Z. Li, T. Yu and Z. Zou, *J. Mater. Chem.*, 2011, **21**, 11347-11351.
159. R. Konta, T. Ishii, H. Kato and A. Kudo, *J. Phys. Chem. B*, 2004, **108**, 8992-8995.
160. J.-P. Zou, L.-Z. Zhang, S.-L. Luo, L.-H. Leng, X.-B. Luo, M.-J. Zhang, Y. Luo and G.-C. Guo, *Int. J. Hydrogen Energy*, 2012, **37**, 17068-17077.
161. H. Tan, Z. Zhao, W.-b. Zhu, E. N. Coker, B. Li, M. Zheng, W. Yu, H. Fan and Z. Sun, *ACS Appl. Mater. Interfaces*, 2014, **6**, 19184-19190.
162. H. Zhang, G. Chen, Y. Li and Y. Teng, *Int. J. Hydrogen Energy*, 2010, **35**, 2713-2716.
163. H. Mizoguchi, K. Ueda, M. Orita, S.-C. Moon, K. Kajihara, M. Hirano and H. Hosono, *Mater. Res. Bull.*, 2002, **37**, 2401-2406.
164. C. Zhen, C. Y. Jimmy, G. Liu and H.-M. Cheng, *Chem. Commun.*, 2014, **50**, 10416-10419.

165. S. Li, J. Zhang, M. G. Kibria, Z. Mi, M. Chaker, D. Ma, R. Nechache and F. Rosei, *Chem. Commun.*, 2013, **49**, 5856-5858.
166. K. Parida, K. Reddy, S. Martha, D. Das and N. Biswal, *Int. J. Hydrogen Energy*, 2010, **35**, 12161-12168.
167. H. Kato and A. Kudo, *Catal. Lett.*, 1999, **58**, 153-155.
168. H. Nakanishi, K. Iizuka, T. Takayama, A. Iwase and A. Kudo, *ChemSusChem*, 2017, **10**, 112-118.
169. H. Kato and A. Kudo, *Catal. Today*, 2003, **78**, 561-569.
170. A. Iwase, H. Kato and A. Kudo, *ChemSusChem*, 2009, **2**, 873-877.
171. C.-C. Hu, Y.-L. Lee and H. Teng, *J. Mater. Chem.*, 2011, **21**, 3824-3830.
172. J. Wang, S. Su, B. Liu, M. Cao and C. Hu, *Chem. Commun.*, 2013, **49**, 7830-7832.
173. Z. Li, Y. Wang, J. Liu, G. Chen, Y. Li and C. Zhou, *Int. J. Hydrogen Energy*, 2009, **34**, 147-152.
174. F. Zhang, A. Yamakata, K. Maeda, Y. Moriya, T. Takata, J. Kubota, K. Teshima, S. Oishi and K. Domen, *J. Am. Chem. Soc.*, 2012, **134**, 8348-8351.
175. A. Kasahara, K. Nukumizu, G. Hitoki, T. Takata, J. N. Kondo, M. Hara, H. Kobayashi and K. Domen, *J. Phys. Chem. A*, 2002, **106**, 6750-6753.
176. D. Yamasita, T. Takata, M. Hara, J. N. Kondo and K. Domen, *Solid State Ionics*, 2004, **172**, 591-595.
177. Higashi, R. Abe, T. Takata and K. Domen, *Chem. Mater.*, 2009, **21**, 1543-1549.
178. K. Maeda, D. Lu and K. Domen, *Angew. Chem. Int. Ed.*, 2013, **52**, 6488-6491.
179. M. Higashi, R. Abe, K. Teramura, T. Takata, B. Ohtani and K. Domen, *Chem. Phys. Lett.*, 2008, **452**, 120-123.
180. B. Siritanaratkul, K. Maeda, T. Hisatomi and K. Domen, *ChemSusChem*, 2011, **4**, 74-78.
181. T. Matoba, K. Maeda and K. Domen, *Chem. - Eur. J.*, 2011, **17**, 14731-14735.
182. K. Maeda, D. Lu and K. Domen, *ACS Catal.*, 2013, **3**, 1026-1033.
183. C. Pan, T. Takata, M. Nakabayashi, T. Matsumoto, N. Shibata, Y. Ikuhara and K. Domen, *Angew. Chem.*, 2015, **54**, 2955-2959.
184. P. Wu, J. Shi, Z. Zhou, W. Tang and L. Guo, *Int. J. Hydrogen Energy*, 2012, **37**, 13704-13710.
185. W. Luo, Z. Li, X. Jiang, T. Yu, L. Liu, X. Chen, J. Ye and Z. Zou, *Phys. Chem. Chem. Phys.*, 2008, **10**, 6717-6723.
186. J. Li, J. Zeng, L. Jia and W. Fang, *Int. J. Hydrogen Energy*, 2010, **35**, 12733-12740.
187. L. Xu, C. Li, W. Shi, J. Guan and Z. Sun, *J. Mol. Catal. A: Chem.*, 2012, **360**, 42-47.
188. Y. Goto, J. Seo, K. Kumamoto, T. Hisatomi, Y. Mizuguchi, Y. Kamihara, M. Katayama, T. Minegishi and K. Domen, *Inorg. Chem.*, 2016, **55**, 3674-3679.
189. J. Seo, Y. Moriya, M. Kodera, T. Hisatomi, T. Minegishi, M. Katayama and K. Domen, *Chem. Mater.*, 2016, **28**, 6869-6876.
190. K. Ueda, T. Minegishi, J. Clune, M. Nakabayashi, T. Hisatomi, H. Nishiyama, M. Katayama, N. Shibata, J. Kubota and T. Yamada, *J. Am. Chem. Soc.*, 2015, **137**, 2227-2230.
191. M. Higashi, Y. Yamanaka, O. Tomita and R. Abe, *APL Mater.*, 2015, **3**, 104418.
192. S. Chen, A. Walsh, X.-G. Gong and S.-H. Wei, *Adv. Mater.*, 2013, **25**, 1522-1539.
193. A. Walsh, S. Chen, S.-H. Wei and X.-G. Gong, *Adv. Energy Mater.*, 2012, **2**, 400-409.
194. J. Chakrabartty, C. Harnagea, M. Celikin, F. Rosei and R. Nechache, *Nat. Photonics*, 2018, **12**, 271-276.

195. F. Zheng, X. Yu, W Huang, J. Zhang, X. Wang, M. Shen, W. Dong, L. Fang, Y. Bai, S. Shen and J. Hao, *J. Mater. Chem. A*, 2014, **2**, 1363-1368.
196. W. Huang, C. Harnagea, D. Benetti, M. Chaker, F. Rosei, and R. Nechache, *J. Mater. Chem. A*, 2017, **5**, 10355-10364.
197. A. Chynoweth, *Phys. Rev.*, 1956, **102**, 705.
198. W.T.H Koch, R. Munser, W. Ruppel and P. Würfel, *Solid State Commun.*, 1975, **17**, 847-850.
199. M. Qin, K. Yao and Y. C. Liang, *Appl. Phys. Lett.*, 2008, **93**, 122904.
200. S. Y. Yang, J. Seidel, S. J. Byrnes, P. Shafer, C. H. Yang, M. D. Rossell, P. Yu, Y. H. Chu, J. F. Scott, J. W. Ager, L. W. Martin and R. Ramesh, *Nat. Nanotechnol.*, 2010, **5**, 143-147.
201. N. Noginova, N. Kukhtarev, T. Kukhtareva, M. A. Noginov, H. J. Caulfield, P. Venkateswarlu, D. Parker and P. P. Banerjee, *J. Opt. Soc. Am. B-Opt. Phys.*, 1997, **14**, 1390-1395.
202. A. M. Glass, D. V. D. Linde and T. J. Negran, *Appl. Phys. Lett.*, 1974, **25**, 233-235.
203. V. S. Dharmadhikari and W. Grannemann, *J. Appl. Phys.*, 1982, **53**, 8988-8992.
204. J. Ihlefeld, N. Podraza, Z. Liu, R. Rai, X. Xu, T. Heeg, Y. Chen, J. Li, R. Collins and J. Musfeldt, *Appl. Phys. Lett.*, 2008, **92**, 142908.
205. S. Y. Yang, L. W. Martin, S. J. Byrnes, T. E. Conry, S. R. Basu, D. Paran, L. Reichertz, J. Ihlefeld, C. Adamo, A. Melville, Y. H. Chu, C. H. Yang, J. L. Musfeldt, D. G. Schlom, J. W. Ager and R. Ramesh, *Appl. Phys. Lett.*, 2009, **95**, 062909.
206. J. He, C. Franchini and J. M. Rondinelli, *Chem. Mater.*, 2017, **29**, 2445-2451.
207. C. Fischer, K. J. Tibbetts, D. Morgan and G. Ceder, *Nat. Mater.*, 2006, **5**, 641-646.
208. O. Isayev, C. Oses, C. Toher, E. Gossett, S. Curtarolo and A. Tropsha, *Nat. Commun.*, 2017, **8**, 15679.
209. Z. Li, Q. Xu, Q. Sun, Z. Hou, and W.-J. Yin, 2018, arXiv:1803.06042.
210. V. M. Goldschmidt, *Naturwissenschaften*, 1926, **14**, 477-485.
211. L. M. Ghiringhelli, J. Vybiral, S. V. Levchenko, C. Draxl and M. Scheffler, *Phys. Rev. Lett.*, 2015, **114**, 105503.